Space Sci Rev (2010) 154: 265–303
DOI 10.1007/s11214-010-9647-x

In-flight Performance and Initial Results of Plasma Energy Angle and Composition Experiment (PACE) on SELENE (Kaguya)

Yoshifumi Saito · Shoichiro Yokota · Kazushi Asamura · Takaaki Tanaka · Masaki N. Nishino · Tadateru Yamamoto · Yuta Terakawa · Masaki Fujimoto · Hiroshi Hasegawa · Hajime Hayakawa · Masafumi Hirahara · Masahiro Hoshino · Shinobu Machida · Toshifumi Mukai · Tsugunobu Nagai · Tsutomu Nagatsuma · Tomoko Nakagawa · Masato Nakamura · Koh-ichiro Oyama · Eiichi Sagawa · Susumu Sasaki · Kanako Seki · Iku Shinohara · Toshio Terasawa · Hideo Tsunakawa · Hidetoshi Shibuya · Masaki Matsushima · Hisayoshi Shimizu · Futoshi Takahashi

Received: 26 August 2009 / Accepted: 15 March 2010 / Published online: 9 April 2010

Y. Saito (✉) · S. Yokota · K. Asamura · T. Tanaka · M.N. Nishino · T. Yamamoto · M. Fujimoto · H. Hasegawa · H. Hayakawa · T. Mukai · M. Nakamura · S. Sasaki · I. Shinohara
Institute of Space and Astronautical Science, Japan Aerospace Exploration Agency, 3-1-1 Yoshinodai, Sagamihara, Kanagawa 229-8510, Japan
e-mail: saito@stp.isas.jaxa.jp

Y. Terakawa · T. Nagai · T. Terasawa · H. Tsunakawa · M. Matsushima · F. Takahashi
Tokyo Institute of Technology, 2-12-1 Ookayama, Meguro-ku, Tokyo 152-8551, Japan

M. Hirahara · M. Hoshino
University of Tokyo, 7-3-1 Hongo, Bunkyo, Tokyo 113-0033, Japan

S. Machida
Kyoto University, Oiwake-machi, Sakyo-ku, Kyoto 606-8502, Japan

T. Nagatsuma
National Institute of Information and Communications Technology, 4-2-1 Nukuikitamachi, Koganei, Tokyo 184-8795, Japan

T. Nakagawa
Tohoku Institute of Technology, Taihaku-ku, Sendai, Miyagi 982-8577, Japan

K.-i. Oyama
National Central University, No. 300, Jhongda Rd., Jhongli City, Taoyuan County 32001, Taiwan (R.O.C.)

E. Sagawa
Research Institute of Telecommunications and Economics, 3-22-1 Toranomon, Minato-ku, Tokyo 105-0001, Japan

Abstract MAP-PACE (MAgnetic field and Plasma experiment—Plasma energy Angle and Composition Experiment) on SELENE (Kaguya) has completed its ∼1.5-year observation of low-energy charged particles around the Moon. MAP-PACE consists of 4 sensors: ESA (Electron Spectrum Analyzer)-S1, ESA-S2, IMA (Ion Mass Analyzer), and IEA (Ion Energy Analyzer). ESA-S1 and S2 measured the distribution function of low-energy electrons in the energy range 6 eV–9 keV and 9 eV–16 keV, respectively. IMA and IEA measured the distribution function of low-energy ions in the energy ranges 7 eV/q–28 keV/q and 7 eV/q–29 keV/q. All the sensors performed quite well as expected from the laboratory experiment carried out before launch. Since each sensor has a hemispherical field of view, two electron sensors and two ion sensors installed on the spacecraft panels opposite each other could cover the full 3-dimensional phase space of low-energy electrons and ions. One of the ion sensors IMA is an energy mass spectrometer. IMA measured mass-specific ion energy spectra that have never before been obtained at a 100 km altitude polar orbit around the Moon. The newly observed data show characteristic ion populations around the Moon. Besides the solar wind, MAP-PACE-IMA found four clearly distinguishable ion populations on the dayside of the Moon: (1) Solar wind protons backscattered at the lunar surface, (2) Solar wind protons reflected by magnetic anomalies on the lunar surface, (3) Reflected/backscattered protons picked-up by the solar wind, and (4) Ions originating from the lunar surface/lunar exosphere.

Keywords Moon · Ion · Electron · Solar wind · Plasma

1 Introduction

Interaction between the solar wind and a solar system object varies largely according to the object's properties, such as the existence of a global intrinsic magnetic field and/or thick atmosphere. The Moon's case is characterized by the absence of both properties. Until recently, understanding of the lunar plasma environment has suffered from a lack of *in situ* measurements of low-energy ions.

The lunar plasma environment was monitored by the lunar orbiters and landers in the 1960s and 1970s (Lyon et al. 1967; Colburn et al. 1967; Anderson et al. 1972; Howe et al. 1974; Neugebauer et al. 1972; Clay et al. 1972; Hills et al. 1972). Although new discoveries concerning the lunar plasma environment were made during this period, an understanding from the plasma physics point of view via three-dimensional particle distribution function data was difficult.

After the 1990s, three spacecraft, Clementine (Nozette et al. 1994), Lunar Prospector (Binder 1998), and SMART-1 (Foing et al. 2006) orbited the Moon. Three-dimensional low-energy electron measurements by Lunar Prospector revealed the lunar plasma environment, including plasma interactions with crustal magnetic fields, surface charging, and wake structure (Lin et al. 1998; Halekas et al. 2001, 2002, 2005, 2008, 2009a, 2009b).

K. Seki
Solar-Terrestrial Environment Laboratory, Nagoya University, 3-13 Honohara, Toyokawa, Aichi 442-8507, Japan

H. Shibuya
Kumamoto University, 2-39-1, Kurokami, Kumamoto 860-8555, Japan

H. Shimizu
Earthquake Research Institute, University of Tokyo, 1-1-1, Yayoi, Bunkyo-ku, Tokyo 113-0032, Japan

Besides the three orbiters, observations by the Wind spacecraft during its Moon fly-by showed features of the lunar wake (Ogilvie et al. 1996). Remote detection of lunar ions by AMPTE/IRM (Hilchenbach et al. 1993), Wind (Mall et al. 1998), and Nozomi (Futaana et al. 2003), lunar electrons by Nozomi (Futaana et al. 2001), and of ULF waves generated by electron beams around the lunar wake by Geotail (Nakagawa et al. 2003) were also reported.

On the other hand, ground-based observations revealed the existence of a tenuous alkali-atmosphere around the Moon at the end of the 1980s. Potter and Morgan (1988) discovered the existence of Na and K atmospheres above the sunlit limb of the Moon for the first time. Since then, several generation mechanisms have been proposed for the rarefied lunar alkali-atmosphere (Stern 1999). Sputtering caused by solar wind ions drew considerable attention, because it produces secondary particles that reflect the lunar surface composition (Elphic et al. 1991). Potter et al. (2000) found that solar photons play a dominant role in the desorption of the lunar alkali-atmosphere. According to them, sputtering of the lunar surface only contributes to the creation of the lunar Na atmosphere by enhancing diffusion of Na to the lunar surface. Sputtered or desorbed particles from the lunar surface are mainly composed of neutrals, which are ionized by solar photons and electrons.

Increasing information about the lunar alkali-atmosphere obtained by ground-based optical observations and new aspects of the plasma environment around the Moon revealed by Lunar Prospector led to high expectations for new *in-situ* plasma measurements around the Moon. MAP-PACE (MAgnetic field and Plasma experiment-Plasma energy Angle and Composition Experiment) on SELENE (SELenological and ENgineering Explorer) was developed in order to make comprehensive three-dimensional plasma measurements around the Moon. Especially, low-energy ion measurements on a lunar orbit were realized more than 30 years after the Apollo period. SELENE was successfully launched on 14 September 2007 by the H2A launch vehicle from Tanegashima Space Center in Japan. SELENE was inserted into a circular lunar polar orbit of 100 km altitude and continued observations for nearly 1.5 years until it hit the Moon on 10 June 2009. During the last 5 months, the orbit was lowered to $\sim$50 km altitude between January 2009 and April 2009 and some orbits had an even lower perilune altitude of $\sim$10 km after April 2009.

Following the launch of SELENE, two Asian Moon orbiters Chinese Chang'E-1 and Indian Chandrayaan-1 were launched on October 24, 2007 and October 22, 2008, respectively. Chang'E-1 made observations mainly at 200 km altitude around the Moon until it hit the Moon on 1 March, 2009. Chandrayaan-1 also made observations mainly at 100 km altitude around the Moon until it was lost on 29 August, 2009. Concerning low-energy ion measurements, the Solar Wind Ion Detector (SWID) on Chang'E-1 and Solar Wind Ion Monitor (SWIM) on Chandrayaan-1 measured solar wind ions around the Moon.

We will present the dayside low-energy ion population newly found in the $\sim$1.5-year observation of SELENE MAP-PACE as well as details of the flight operation and flight performance of the MAP-PACE sensors.

2 Instrument Description and Pre-flight Calibration

2.1 Overview

MAP-PACE consists of 4 sensors, ESA (Electron Spectrum Analyzer)-S1, ESA-S2, IMA (Ion Mass Analyzer) and IEA (Ion Energy Analyzer). ESA-S1 and ESA-S2 measure the three-dimensional distribution function of low-energy electrons below 16 keV, while IMA and IEA measure the three-dimensional distribution function of low-energy ions below

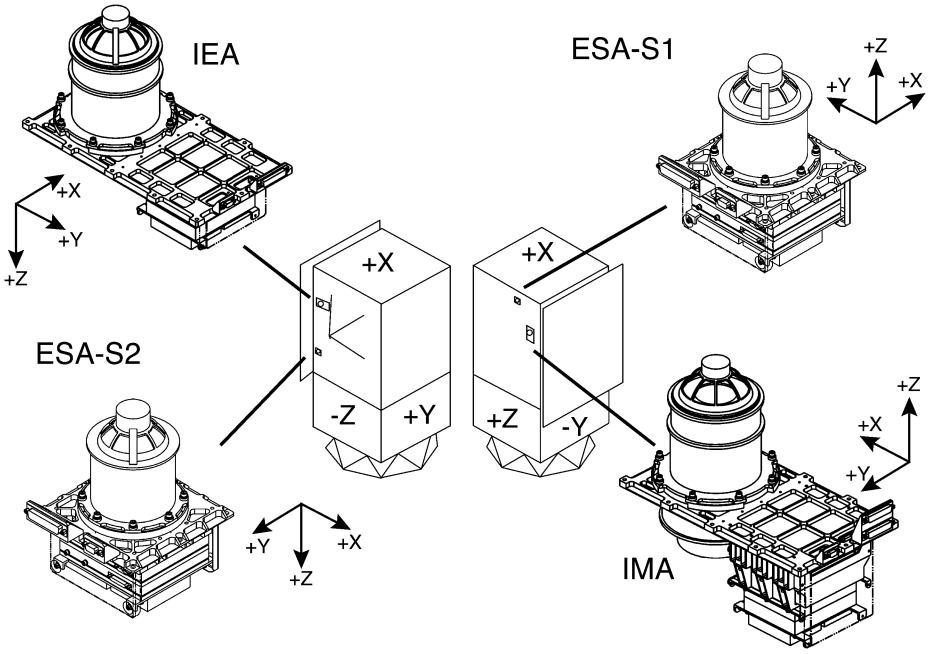

Fig. 1 MAP-PACE sensors on SELENE. The +Z panel of SELENE on which IMA and ESA-S1 were installed always faced the lunar surface. The axis of symmetry in the field of view of ESA-S1 and IMA was the +Z direction while that of ESA-S2 and IEA was the −Z direction

29 keV/q. IMA is an LEF-TOF (Linear Electric Field-Time Of Flight) energy mass spectrometer capable of identifying ion species with mass number up to ∼60 (Yokota et al. 2005). Figure 1 shows a schematic drawing of the PACE sensors on SELENE. Since SELENE is a three-axis stabilized spacecraft that keeps one of its spacecraft panels (+Z panel) facing the Moon, a pair of sensors (ESA-S1 and ESA-S2 for electrons and IMA and IEA for ions), having hemispherical fields of view in opposite directions to each other, are necessary for obtaining three-dimensional particle distribution functions.

Figure 2 shows a functional block diagram of MAP-PACE. MAP is composed of two subsystems MAP-PACE (Saito et al. 2007, 2008a) and MAP-LMAG (Lunar MAGnetometer) (Shimizu et al. 2008; Takahashi et al. 2009). In order to minimize the mass and power, the control electronics for the MAP-PACE sensors and MAP-LMAG sensors are contained in one package, MAP-E (MAgnetic field and Plasma experiment-Electronics). Detected electron/ion signals are pre-amplified and transmitted from each sensor to MAP-E which includes a position detection circuit, TOF measurement circuit and count RAMs. MAP-E also controls high voltage power supplies in each sensor head with analog signals. MAP-PACE sensors are controlled by a CPU board called SI-OBC (Science Instrument-OnBoard Computer). MAP-E also consists of another CPU board called TC-OBC (Telemetry Command-OnBoard Computer) which is responsible for interfacing with spacecraft via a 1553B interface.

2.2 ESA-S1 and ESA-S2

ESA-S1 and ESA-S2 are top hat type electrostatic analyzers (Carlson et al. 1982) with FOV (Field Of View) scanning deflectors at the entrance and toroidal electrodes inside (see

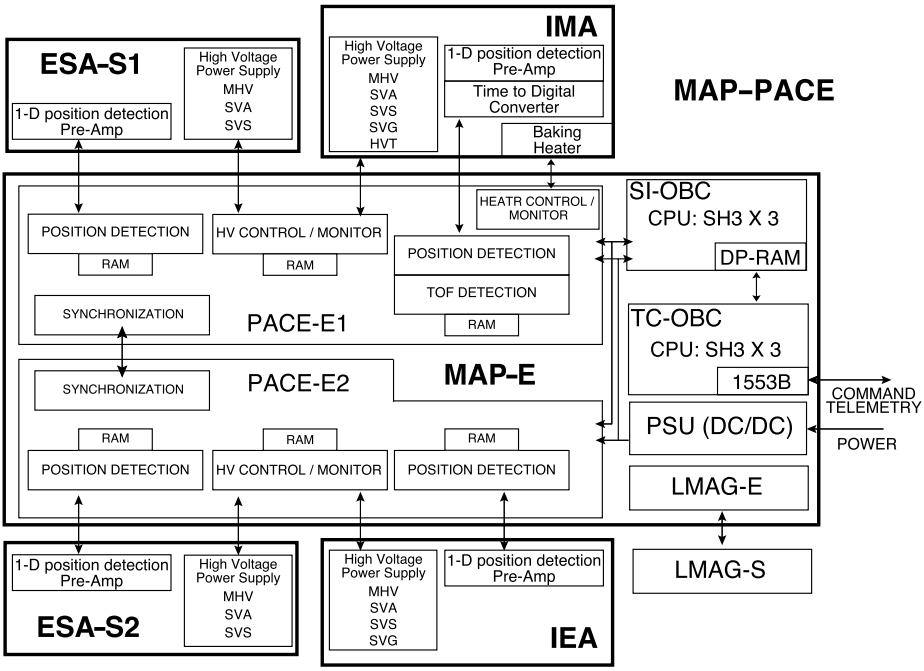

Fig. 2 Functional block diagram of MAP-PACE. The acronyms in the figure are as follows: MHV (MCP High Voltage), SVA (Sweep high Voltage for Angular scanning deflector), SVS (Sweep high Voltage for Spherical deflector), SVG (Sweep high Voltage for Geometrical factor control), HVT (High VolTage for LEF), RAM (Random Access Memory), HV (High Voltage), TOF (Time Of Flight), SI-OBC (Science Instrument-On Board Computer), TC-OBC (Telemetry Command-On Board Computer), CPU (Central Processing Unit), DP-RAM (Dual Port-Random Access Memory), PSU (Power Supply Unit), DC/DC (DC/DC converter), LMAG-E (Lunar MAGnetometer-Electronics), LMAG-S (Lunar MAGnetometer-Sensor), ESA-S1 (Electron Spectrum Analyzer-S1), ESA-S2 (Electron Spectrum Analyzer-S2), IMA (Ion Mass Analyzer), IEA (Ion Energy Analyzer), MAP-E (Magnetic field And Plasma experiment-Electronics), PACE-E1 (Plasma energy Angle and Composition Experiment-Electronics1), PACE-E2 (Plasma energy Angle and Composition Experiment-Electronics2)

Fig. 3). The FOV is electrically scanned between ± 45 degrees around the center of the FOV, which is 45 degrees inclined from the axis of symmetry. The three-dimensional electron distribution function is observed with two ESA sensors that are installed on the $+Z$ (ESA-S1: nadir-looking) and $-Z$ (ESA-S2: zenith-looking) panels of the spacecraft. The curved upper and lower FOV scanning deflectors are supplied with high voltages which are swept between 0 V and $+4$ kV. The inner toroidal electrode is also supplied with a high voltage swept between 0 V and $+3$ kV simultaneously with the FOV scanning deflectors. The electrons that pass through the FOV scanning deflectors enter into the toroidal deflectors. Only electrons in a specific energy range can travel further down to the exit of the toroidal deflectors. The electrons that pass through the toroidal deflectors enter a Micro-Channel Plate (MCP) and are intensified to detectable charge pulses. Between the toroidal deflectors and MCP, there exists a slit and grid supplied with a slightly negative voltage (-4.0 V) in order to reject the secondary electrons that give spurious counts. The charge pulses intensified by the MCP are received by a one-dimensional circular resistive anode. The positions where the charge pulses are detected correspond to the incident azimuthal directions of the electrons. Since the gap between the toroidal deflectors of ESA-S1 is larger than that of ESA-S2, the max-

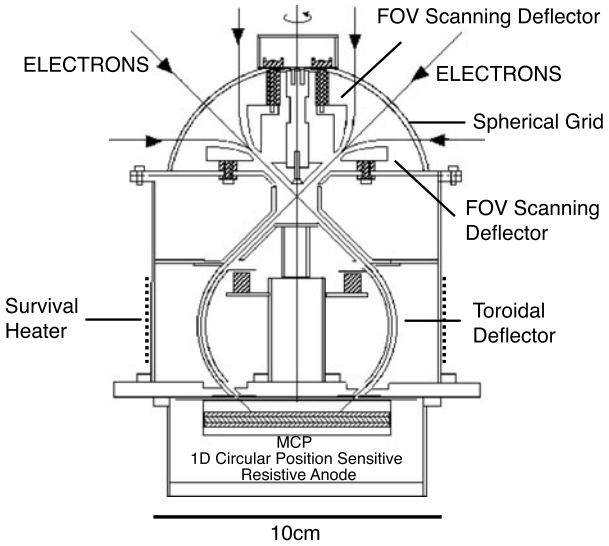

Fig. 3 Cross section of ESA-S1 and ESA-S2

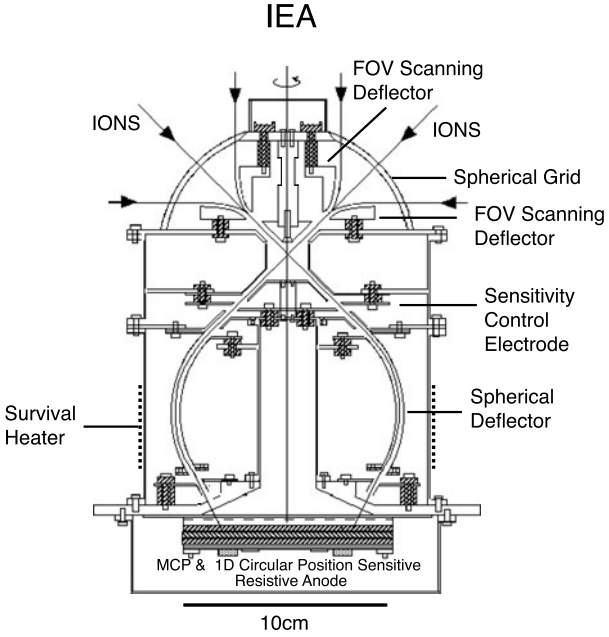

Fig. 4 Cross section of IEA

imum energy and energy resolution of ESA-S1 is lower than ESA-S2 while the g-factor of ESA-S1 is larger than ESA-S2 (see Table 1).

2.3 IMA and IEA

IMA consists of an energy analyzer which has a similar structure to the ESA sensors and an LEF (Linear Electric Field) TOF (Time Of Flight) ion mass analyzer (McComas and Nordholt 1990; Yokota and Saito 2005; Yokota et al. 2005). IEA consists only of an energy

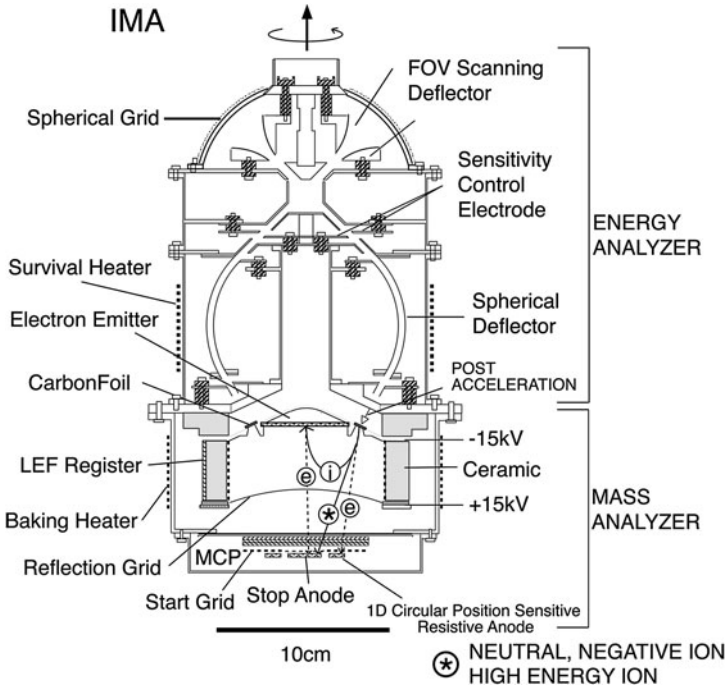

Fig. 5 Cross section of IMA

analyzer which is the same as the energy analyzer of IMA (see Fig. 4 and Fig. 5). IMA is installed on the +Z (nadir-looking) panel while IEA is installed on the −Z (zenith-looking) panel. The curved upper and lower FOV scanning deflectors of the energy analyzer are supplied with a high voltage which is swept between 0 V and +4.2 kV. The inner spherical deflector is also supplied with a high voltage swept between 0 V and −4 kV simultaneously with the FOV scanning deflectors. Between the spherical deflector and the FOV scanning deflectors, there exists a pair of electrodes that serve as sensitivity control electrodes. When a high positive voltage is applied to these electrodes, a potential barrier that obstructs the passage of ions is formed (Yokota et al. 2005). Since the fluxes of the solar wind ions and the ions coming from the Moon differ significantly, the sensitivity of the energy analyzer is reduced to about 1/50 for solar wind ion observation. The ions transmitted through the energy analyzer of IEA are detected by an MCP with one-dimensional circular resistive anode. The ions transmitted through the energy analyzer of IMA are post accelerated by −15 kV and enter into the LEF TOF mass analyzer part. Thin carbon foils (0.5 μg/cm^2) are placed at the entrance of the LEF TOF mass analyzer, which generate start electrons when ions pass through the carbon foil. The start electrons are accelerated by the electric field inside the mass analyzer and their positions are detected by a one-dimensional circular resistive anode that placed behind the MCP (Yokota and Saito 2008). These start electrons also generate start signals when they pass through a grid anode positioned between the position-sensitive anode and the MCP. Most of the ions that pass through the carbon foil lose their initial charge state and enter into the mass analyzer as neutral particles. These neutral particles are detected by an anode that is in the center of the position sensitive anode. These signals are used as stop signals. The mass/charge of the incident ions can be calculated from their energy/charge and the time of flight. Some of the incident ions enter the time-of-flight section as ions. These

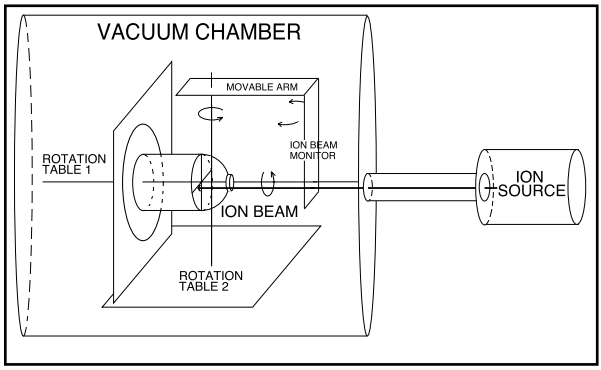

Fig. 6 Configuration of pre-flight calibration experiment

ions are reflected by the linear electric field whose intensity is proportional to the distance from the entrance point. The reflected ions generate secondary electrons when they collide with the top part of the mass analyzer where a MgO coated aluminum plate is installed in order to increase the secondary electron yield (Tanaka and Saito 2009). The generated electrons are accelerated and detected by the center anode, which generates stop signals. For the ions, the time-of-flight section of IMA acts as a so-called "isochronous time-of-flight" to first order of energy deviation. To first order of energy deviation, the time of flight of the reflected ions is proportional to the square root of the ion mass. Therefore the mass of the incident ions can be determined without being significantly affected by the angular scattering and energy degradation caused by ion passage in the carbon foil (McComas and Nordholt 1990; Yokota et al. 2005). With this design of LEF-TOF mass spectrometer, the center anode detects both neutrals (direct time-of-flight) and secondary electrons from the top part of the mass analyzer, generated by ions (isochronous time-of-flight). We have measured the time profile of several ion species by injecting those ions into IMA. Each ion species has its own characteristic TOF profile including neutral peak, ion peak and/or negative ion peak (Yokota et al. 2005). Since some of these TOF profiles overlap with each other, we have to use a deconvolution tool devised from calibration data of TOF profiles in order to determine the mass of the measured ions if a number of species exists simultaneously (Yokota et al. 2005). The instrument sensitivity for heavy ions such as Fe^+ is relatively low because most of the incident Fe^+ ions are converted to neutrals when they pass through the carbon foil and the angular scattering/energy straggling which affects the detection efficiency of the direct time-of-flight is more significant for heavy ions.

2.4 Pre-flight Calibration

Pre-flight calibration of the PACE sensors were carried out at a calibration facility in the Institute of Space and Astronautical Science/Japan Aerospace Exploration Agency (Wüest et al. 2007). The PACE sensors were installed in a vacuum chamber one by one and nitrogen ions were injected. In order to obtain the time profile of the TOF-analyzed ions with IMA, we also used hydrogen, helium, carbon, oxygen and heavier ions such as sodium and chlorine. Figure 6 shows schematically the configuration of the calibration experiment. The sensor under calibration was installed on a "rotation table 1" which had a rotation axis parallel to the sensor's axis of rotational symmetry. The "rotation table 1" was installed on "rotation table 2" whose rotation axis was perpendicular to that of "rotation table 1". The ion beam profile was intermittently monitored by an MCP with a position-sensitive anode that was

Table 1 Characteristics of ESA-S1 and ESA-S2

	ESA-S1	ESA-S2
Energy Range	6 eV–9 keV	9 eV–16 keV
Energy Resolution (FWHM)	15%	10%
Energy Sweep Step	32	32
Field of View	2π str.	2π str. (< 9 keV)
FOV Sweep range	45°±45°(Pol)	45°±45°(Pol)
Angular Resolution (FWHM)	5°(Pol)×8°(Az)	5°(Pol)×8°(Az)
g-factor (5.625° on MCP) (max.)	5.3×10^{-4}	1.2×10^{-4}
(efficiency is not included)	cm^2 str keV/keV	cm^2 str keV/keV
Time Resolution (3D) (min.)	1 second	1 second
Analyzer Type	toroidal analyzer	toroidal analyzer
average radius	30 mm	30 mm
gap	5 mm	3 mm
eccentricity	5 mm	5 mm

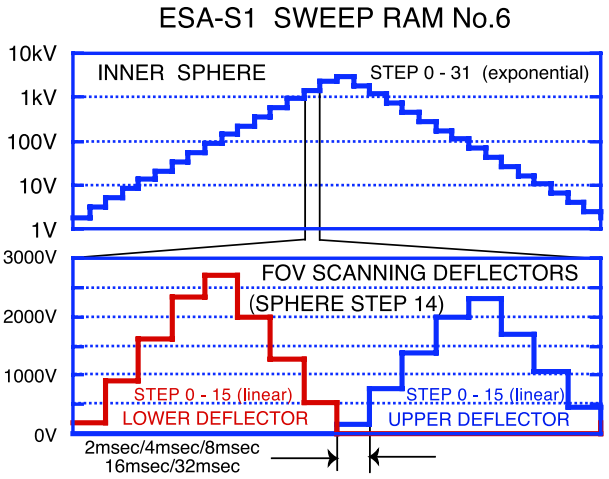

Fig. 7 High-voltage sweep waveforms applied to the inner sphere and FOV scanning deflectors of ESA-S1. Duration of the FOV scanning deflectors' step can be selected from 2 ms, 4 ms, 8 ms, 16 ms and 32 ms

installed on a movable arm. Most of the data were obtained using 6 keV ion beams since the beam profile was uniform and stable. In measuring the performance of the sensitivity controlling electrode, lower energy ions of 2 keV were used.

2.4.1 Instrument Performance of ESA-S1 and ESA-S2

Table 1 summarizes the characteristics of ESA-S1 and ESA-S2. Figure 7 shows an example of the high-voltage sweep waveforms applied to the inner sphere and FOV scanning deflectors of ESA-S1. The high voltage waveforms applied to the inner sphere and FOV scanning deflectors of ESA-S2 were similar to those of ESA-S1. The measurement energy range was divided into 32 steps and in each step, 16 polar angle directions were swept by applying a high positive voltage to the upper or lower deflectors. A high positive voltage was used in order to prevent photoelectron beams from being emitted from the FOV scanning deflectors.

Table 2 Average measurement energy of ESA-S1

STEP	SWEEP RAM No.6 (keV)			SWEEP RAM No.0 (keV)		
	min.	center	max.	min.	center	max.
0	0.0049	0.0055	0.0064	0.0886	0.0999	0.1159
1	0.0081	0.0091	0.0105	0.2696	0.3042	0.3530
2	0.0132	0.0149	0.0173	0.3607	0.4069	0.4722
3	0.0208	0.0235	0.0273	0.1785	0.2014	0.2337
4	0.0340	0.0384	0.0445			
5	0.0544	0.0614	0.0713			
6	0.0875	0.0987	0.1146			
7	0.1405	0.1585	0.1839			
8	0.2263	0.2553	0.2962			
9	0.3632	0.4097	0.4754			
10	0.5845	0.6595	0.7652			
11	0.9395	1.0600	1.2301			
12	1.4992	1.6915	1.9628			
13	2.4050	2.7135	3.1488			
14	3.8501	4.3439	5.0406			
15	6.2486	7.0237	8.1119			
16	7.7892	8.8106	10.2475			
17	4.8725	5.4974	6.3792			
18	3.0400	3.4299	3.9800			
19	1.8923	2.1350	2.4774			
20	1.1782	1.3294	1.5426			
21	0.7389	0.8337	0.9674			
22	0.4588	0.5177	0.6007			
23	0.2849	0.3214	0.3730			
24	0.1777	0.2005	0.2326			
25	0.1101	0.1242	0.1442			
26	0.0693	0.0782	0.0908			
27	0.0431	0.0486	0.0564			
28	0.0266	0.0300	0.0348			
29	0.0166	0.0188	0.0218			
30	0.0106	0.0119	0.0138			
31	0.0063	0.0071	0.0082			

In order to measure the same polar direction with different energy, the high voltage applied to the FOV scanning deflectors should be proportional to the high voltage applied to the inner sphere. Although ESA-S1 and ESA-S2 had 8 different energy sweep modes, only two ("SWEEP RAM No.0" and "SWEEP RAM No.6") were actually used. Tables 2 and 3 show the average measurement energy of ESA-S1 and ESA-S2 for these two energy sweep modes. One of the energy sweep modes "SWEEP RAM No.0" had only 4 energy steps. This energy sweep mode was used for Electron Reflectometer measurements. In order to increase the time resolution (spatial resolution) when detecting magnetic anomalies on the lunar surface, 4 energy steps were repeated 8 times instead of sweeping 32 different energy steps.

Table 3 Average measurement energy of ESA-S2

STEP	SWEEP RAM No.6 (keV)			SWEEP RAM No.0 (keV)		
	min.	center	max.	min.	center	max.
0	0.0085	0.0092	0.0100	0.0902	0.0978	0.1065
1	0.0145	0.0158	0.0172	0.2759	0.2993	0.3258
2	0.0240	0.0261	0.0284	0.3686	0.3998	0.4353
3	0.0380	0.0412	0.0448	0.1822	0.1976	0.2151
4	0.0623	0.0676	0.0735			
5	0.0997	0.1082	0.1178			
6	0.1605	0.1740	0.1895			
7	0.2607	0.2828	0.3079			
8	0.4212	0.4568	0.4974			
9	0.6763	0.7336	0.7987			
10	1.0850	1.1769	1.2814			
11	1.6781	1.8201	1.9818			
12	2.7312	2.9624	3.2254			
13	4.3640	4.7334	5.1538			
14	7.0631	7.6567	8.3282			
15	11.2811	12.2496	13.3516			
16	14.2690	15.4980	16.9026			
17	8.9223	9.6784	10.5461			
18	5.5487	6.0184	6.5528			
19	3.4515	3.7437	4.0762			
20	2.1414	2.3227	2.5289			
21	1.3736	1.4899	1.6222			
22	0.8559	0.9284	1.0108			
23	0.5329	0.5780	0.6293			
24	0.3301	0.3581	0.3899			
25	0.2053	0.2227	0.2425			
26	0.1271	0.1378	0.1501			
27	0.0794	0.0861	0.0937			
28	0.0488	0.0529	0.0576			
29	0.0304	0.0330	0.0359			
30	0.0190	0.0207	0.0225			
31	0.0113	0.0123	0.0134			

Figure 8 shows examples of the geometrical factor of ESA-S1 (1.3 keV electrons) and ESA-S2 (2.3 keV electrons). The geometrical factor is shown on a color map relative to azimuthal direction (channels) and polar direction. Since there were some directions with no sensitivity due to the existence of "supports" for the spherical grid in the entrance region, the geometrical factor was not uniform in the hemispherical FOV. Due to the existence of an upper limit for the high voltage applied to the FOV scanning deflectors, high-energy electrons above 9 keV could not be fully deflected. Therefore ESA-S2 had an energy dependence for the geometrical factor, especially for the 3 highest energy steps when using "SWEEP RAM No.6". Figure 9 shows examples of angular coverage of ESA-S1 (1.3 keV electrons) and

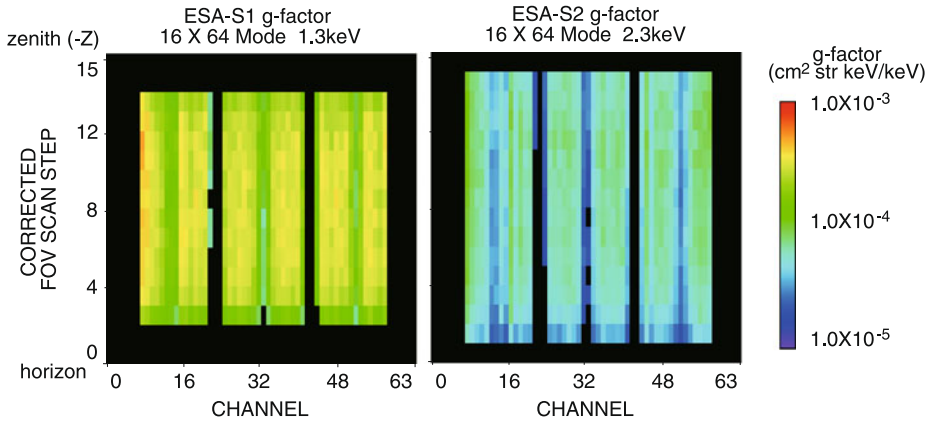

Fig. 8 Geometrical factor of ESA-S1 and ESA-S2. Geometrical factor relative to azimuthal channels and FOV scan steps is shown on a color map. Geometrical factor of each channel is shown sequentially from horizontal direction to zenith direction. *Black color* indicates no sensitivity

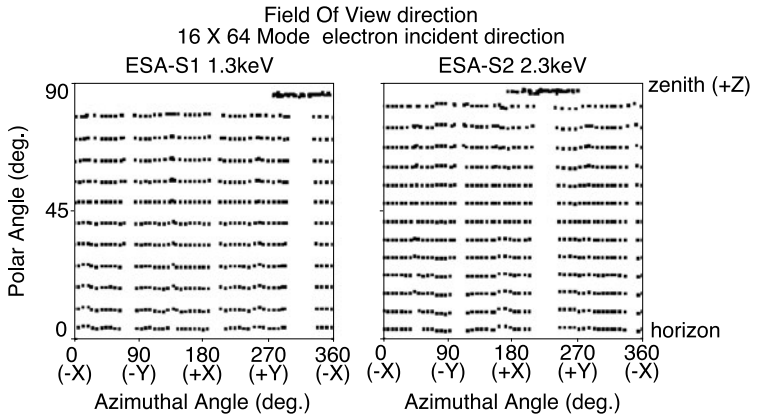

Fig. 9 Angular coverage of ESA-S1 and ESA-S2. The center of the angular sampling points are indicated by *small dots*. Although the angular sampling points with polar angle ∼90° (zenith direction of the hemispherical FOV) seem to be concentrated between 270° and 360° for ESA-S1 and between 180° and 270° for ESA-S2, this is an artificial effect when calculating the center of the sampling points because electrons from the zenith direction enter uniformly relative to the azimuthal direction (channels)

ESA-S2 (2.3 keV electrons). The center of the angular sampling points are indicated by small dots. Although the angular sampling points with polar angle ∼ 90° (zenith direction of the hemispherical FOV) seem to be concentrated between 270° and 360° for ESA-S1 and between 180° and 270° for ESA-S2, this is an artificial effect when calculating the center of the sampling points because electrons from the zenith direction enter uniformly relative to the azimuthal direction (channels).

2.4.2 Instrument Performance of IEA

The characteristics of IEA are summarized in Table 4. Figure 10 shows an example of the high-voltage sweep waveforms applied to the inner sphere, FOV scanning deflectors and

Table 4 Characteristics of IEA and IMA

	IEA	IMA
Energy Range	7 eV/q–29 keV/q	7 eV/q–28 keV/q
Energy Resolution (FWHM)	5%	5%
Energy Sweep Step	32	32
Mass Range		1–60
Mass Resolution (max.)		m/Δm$\sim$15
Field of View	2π str.($<$ 7 keV/q)	2π str.($<$ 7 keV/q)
FOV Sweep range	45°$\pm$45°(Pol)	45°$\pm$45°(Pol)
Angular Resolution (FWHM)	5°(Pol)$\times$5°(Az)	5°(Pol)$\times$10°(Az)
g-factor (5.625° on MCP) (max.)	2.1×10^{-4} (atten.:off)	4.5×10^{-4}
(efficiency is not included)	cm^2 str keV/keV	cm^2 str keV/keV
	3.8×10^{-6}(atten.:on)	
	cm^2 str keV/keV	
Time Resolution (3D) (min.)	1 second	1 second
Analyzer Type	spherical analyzer	spherical analyzer
average radius	55 mm	55 mm
gap	4 mm	4 mm

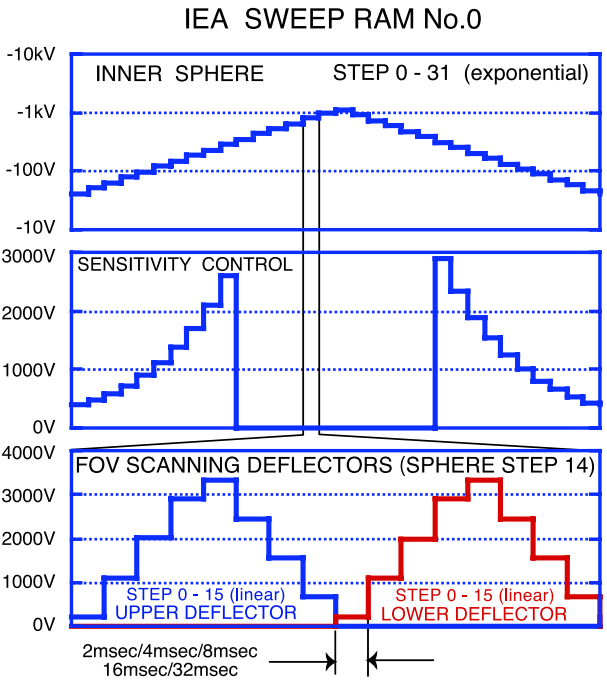

Fig. 10 High-voltage sweep waveforms applied to the inner sphere, sensitivity control electrode and FOV scanning deflectors of IEA. Duration of the FOV scanning deflectors' step can be selected from 2 ms, 4 ms, 8 ms, 16 ms and 32 ms

sensitivity control electrodes of IEA. The measurement energy range was divided into 32 steps and in each step 16 polar angle directions were swept by applying a high positive voltage to the upper or lower deflectors. In one of the energy sweep modes, "SWEEP RAM

Table 5 Average measurement energy of IEA

STEP	SWEEP RAM No.0 (keV)			SWEEP RAM No.1 (keV)		
	min.	center	max.	min.	center	max.
0	0.2799	0.3180	0.3336	0.0061	0.0065	0.0070
1	0.3487	0.3961	0.4156	0.0101	0.0108	0.0117
2	0.4323	0.4911	0.5153	0.0185	0.0198	0.0214
3	0.5328	0.6053	0.6351	0.0330	0.0354	0.0382
4	0.6623	0.7524	0.7894	0.0573	0.0614	0.0663
5	0.8181	0.9294	0.9751	0.0991	0.1063	0.1146
6	1.0131	1.1509	1.2074	0.1693	0.1814	0.1957
7	1.2545	1.4252	1.4952	0.2880	0.3086	0.3329
8	1.5419	1.7516	1.8377	0.4903	0.5255	0.5668
9	1.9054	2.1646	2.2710	0.8343	0.8941	0.9645
10	2.3464	2.5147	2.7126	1.4271	1.5295	1.6499
11	2.9075	3.1161	3.3613	2.4435	2.6188	2.8249
12	3.5954	3.8533	4.1566	4.1647	4.4634	4.8147
13	4.4520	4.7713	5.1468	6.9811	7.4819	8.0707
14	5.5075	5.9025	6.3671	11.8786	12.8131	13.9184
15	6.7902	7.2773	7.8501	20.2672	21.8378	23.7430
16	7.5246	8.0812	8.7265	26.6020	28.6687	31.1534
17	6.1084	6.5466	7.0618	15.5357	16.7531	18.2105
18	4.9436	5.2982	5.7153	9.0752	9.7861	10.6166
19	4.0035	4.2906	4.6283	5.3921	5.7789	6.2338
20	3.2258	3.4572	3.7293	3.1962	3.4254	3.6950
21	2.6229	2.8110	3.0323	1.8689	2.0029	2.1606
22	2.1091	2.3960	2.5138	1.0906	1.1688	1.2608
23	1.7145	1.9477	2.0435	0.6360	0.6816	0.7353
24	1.3732	1.5600	1.6367	0.3777	0.4048	0.4366
25	1.1277	1.2811	1.3441	0.2219	0.2378	0.2565
26	0.9126	1.0367	1.0877	0.1295	0.1388	0.1497
27	0.7345	0.8344	0.8754	0.0755	0.0810	0.0873
28	0.5935	0.6743	0.7074	0.0445	0.0477	0.0515
29	0.4809	0.5463	0.5732	0.0250	0.0267	0.0288
30	0.3892	0.4421	0.4638	0.0142	0.0152	0.0164
31	0.3109	0.3532	0.3706	0.0081	0.0087	0.0094

No.0", the sensitivity of IEA was reduced to ∼1/50 below 2.4 keV/q by applying a high positive voltage to the sensitivity control electrode as shown in Fig. 10. The high voltages applied to the FOV scanning deflectors and sensitivity control electrodes were proportional to the high voltage applied to the inner sphere. Although IEA had 4 different energy sweep modes, only two were actually used. Table 5 shows the average measurement energy of IEA for these two energy sweep modes. "SWEEP RAM No.0" had a narrower energy range with sensitivity attenuation which was used for observing solar wind ions while "SWEEP RAM No.1" had a wider energy range with no sensitivity attenuation.

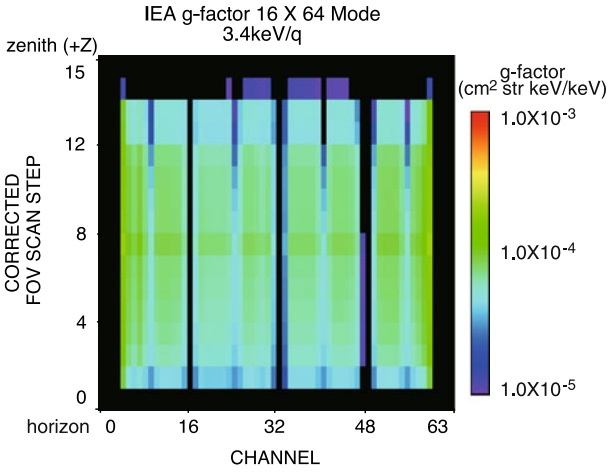

Fig. 11 Geometrical factor of IEA

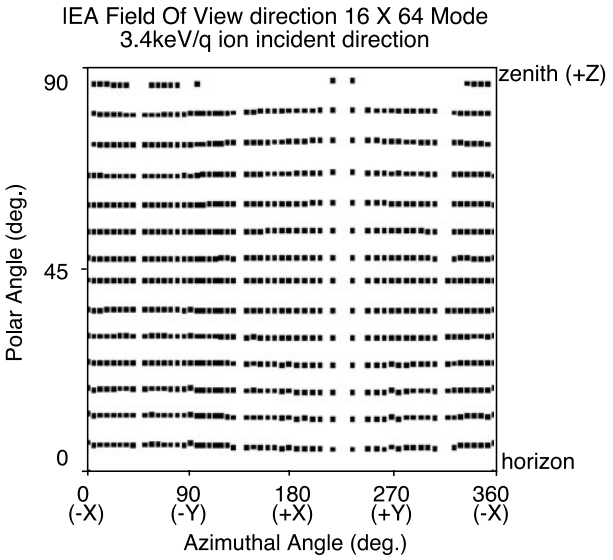

Fig. 12 Angular coverage of IEA

Figure 11 shows an example of the geometrical factor of IEA (3.4 keV/q ions). Similar to the geometrical factor of ESA-S1 and ESA-S2, the geometrical factor of IEA was not uniform in the hemispherical FOV. Since there exists an upper limit to the high voltage that can be applied to the FOV scanning deflectors, high-energy ions could not be fully deflected. Therefore there exists an energy dependence in the geometrical factor especially for the two highest energy steps when using "SWEEP RAM No.0" and the 6 highest energy steps when using "SWEEP RAM No.1". Figure 12 shows an example of the angular coverage of IEA (3.4 keV/q ions).

2.4.3 Instrument Performance of IMA

The characteristics of IMA are summarized in Table 4. The high voltage waveforms applied to the inner sphere and FOV scanning deflectors of IMA were similar to those of IEA.

Table 6 Average measurement energy of IMA

SWEEP RAM No.0 No.1 (keV)			
STEP	min.	center	max.
0	0.0066	0.0070	0.0075
1	0.0097	0.0103	0.0111
2	0.0181	0.0192	0.0208
3	0.0322	0.0342	0.0370
4	0.0552	0.0588	0.0636
5	0.0967	0.1029	0.1113
6	0.1663	0.1769	0.1915
7	0.2846	0.3028	0.3277
8	0.4854	0.5164	0.5588
9	0.8275	0.8804	0.9527
10	1.4171	1.5076	1.6314
11	2.4272	2.5822	2.7942
12	4.1404	4.4049	4.7664
13	6.9922	7.4388	8.0494
14	11.8547	12.6345	13.7163
15	20.3676	21.6846	23.5519
16	26.7004	28.3839	30.8333
17	15.5942	16.6045	18.0305
18	9.1031	9.7197	10.5531
19	5.3202	5.6600	6.1246
20	3.1716	3.3742	3.6511
21	1.8559	1.9744	2.1365
22	1.0831	1.1523	1.2469
23	0.6321	0.6725	0.7277
24	0.3739	0.3978	0.4304
25	0.2191	0.2330	0.2522
26	0.1271	0.1352	0.1463
27	0.0737	0.0784	0.0848
28	0.0427	0.0454	0.0491
29	0.0244	0.0260	0.0281
30	0.0139	0.0148	0.0160
31	0.0081	0.0086	0.0093

Although IMA also could reduce the sensitivity by applying a high voltage to the sensitivity control electrodes, this function was not used during actual operation. Since IMA had a more complicated structure than IEA, the ion detection efficiency of IMA was lower than that of IEA. Table 6 shows the measurement energy of IMA. There was no difference between the two energy sweep modes “SWEEP RAM No.0” and “SWEEP RAM No.1” for IMA.

Figure 13 shows the geometrical factor of IMA. The geometrical factor of IMA also is not uniform in the hemispherical FOV. Similarly to IEA, there exists an upper limit to the high voltage that can be applied to the FOV scanning deflectors, which leads to a partial deflection of high-energy ions. Therefore there exists an energy dependence in the geomet-

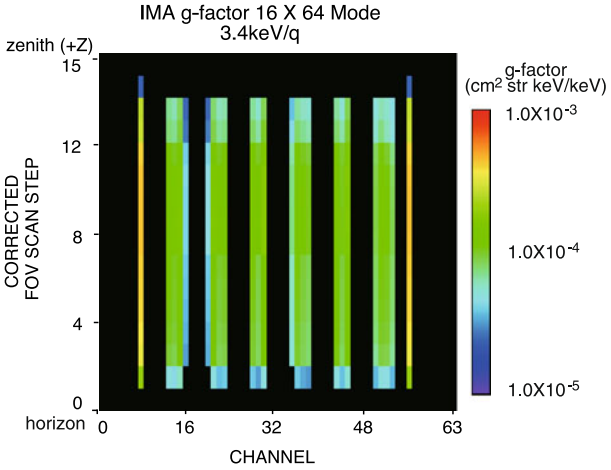

Fig. 13 Geometrical factor of IMA

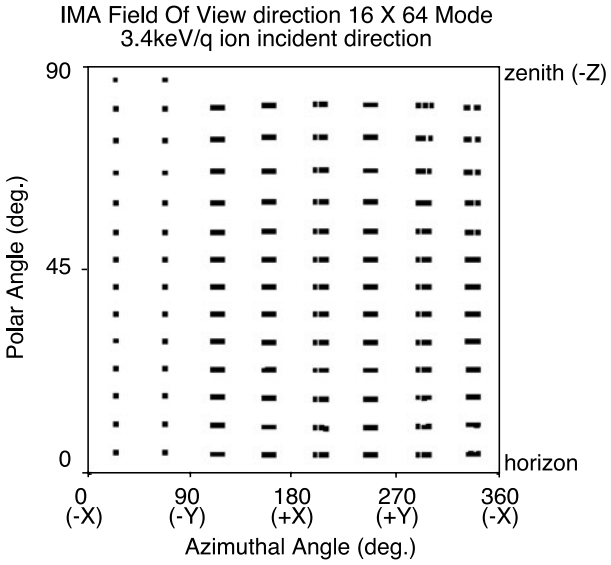

Fig. 14 Angular coverage of IMA

rical factor especially for the 6 highest energy steps when using both "SWEEP RAM No.0" and "SWEEP RAM No.1". Figure 14 shows the angular coverage of IMA. Due to the focusing effect of the start electrons whose position determined the azimuthal direction of the incident ions, the azimuthal angular sampling points were not equally distributed.

The mass detection performance of IMA was measured using hydrogen, helium, carbon, oxygen and heavier ions such as sodium and chlorine. Figure 15 shows an example of the TOF mass profile of IMA obtained during pre-flight calibration. We applied ± 12 kV to the LEF part of IMA and injected 8 keV ion beams of each species one by one. The ion species and charge state after passing through the carbon foil are indicated in the figure. Counts of each species are normalized to peak count. The time measurement resolution was 4 ns as indicated in the figure. Numerically simulated peak positions are also indicated

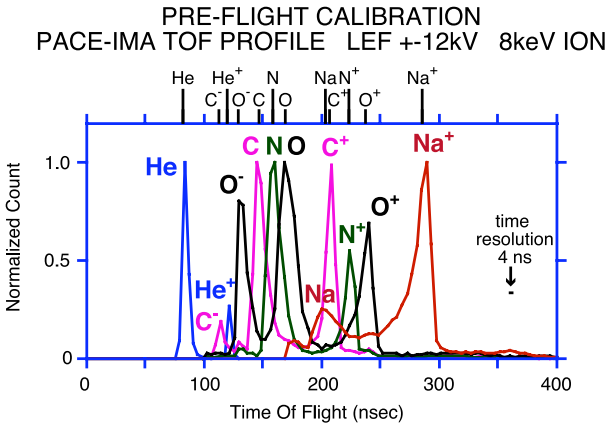

Fig. 15 TOF mass profile of IMA measured during the pre-flight test. Ion species and charge state after passing through the carbon foil are indicated. Counts of each species are normalized by peak count. Time measurement resolution was 4 ns as indicated in the figure. Applied voltage to the LEF register was ± 12 kV and the beam energy was 8 keV. Numerically simulated peak positions are also indicated in the upper part of the figure

in the upper part of the figure. The numerically simulated peaks correspond well with the measured peaks.

3 Onboard Data Processing

Since the telemetry rate allocated to MAP-PACE (42 kbps) was much lower than its raw data rate, the onboard computer SI-OBC (see Fig. 2) reduced the quantity of data in order that the data sent to the ground would fit into the allocated telemetry rate. Data processing includes data compression, pitch angle sorting of electron data, integrating mass channels and angular sectors and selecting the angular sampling points of the solar wind ions by tracking solar wind direction. A reversible data compression algorithm, arithmetic compression, was used for data compression.

We had several operation modes in order to send optimized data within the allocated telemetry rate. Table 7 shows operation modes used during the flight. Although we prepared much more operation modes than shown in Table 7, we did not use some of them. Mode 12 is called "High-angular resolution Mode". In this mode, all the sensors had high-angular resolution with the hemispherical FOV divided into 16 polar and 64 azimuthal sectors. Although the angular resolution was high, the time resolution was as low as 16 seconds. IMA sent no mass information in this mode. Mode 11 is called "TOF Profile Mode". In this operation mode, IMA sent the detailed TOF mass profile (1024 mass data) at the expense of low-angular resolution (only 4 polar angle sectors and no azimuthal angle sectors) and a low time resolution of 32 seconds. The time resolution and angular resolution of IEA were also low when the data were obtained by dividing the hemispherical FOV into 4 polar and 16 azimuthal sectors with a time resolution of 32 seconds. Electron data in this operation mode were the same as Mode 12. Mode 13 is called "Highest Time Resolution Mode" and was mainly used for monitoring the sensor condition when changing the high voltage level with a time resolution of 1 second for IEA and IMA and 2 seconds for ESA-S1 and ESA-S2. In this mode, all the sensors had low-angular resolution with the hemispherical FOV divided into 4 polar and 16 azimuthal sectors. IMA sent no mass information in this mode. Mode 14(24) is called "High Time Resolution Mode". Since the electron and ion distributions on the dayside and nightside were quite different, Mode 14 was optimized for dayside observation while Mode 24 was optimized for nightside observation. Switching between Mode 14 and Mode 24 was done with commands from the ground or by onboard time sequence

Table 7 PACE operation modes used during flight

No.	Mode Name	ER /3D	Electron Data (P×Az×E)	Te (sec)	Ion Data (P×Az×E×M)	Ti (sec)
11	TOF Profile	3D	32×64×32	16	IEA : 4×16×32×1 IMA : 4×1×32×1024	32 32
12	High Angular Resolution	3D	32×64×32	16	32×64×32×1	16
13	Highest Time Resolution	3D	8×16×32	2	8×16×32×1	1
14(S)		3D	8×16×32	2	IEA : 128(16×64)×32×1	2
	High Time				IMA : 4×16×32×8	8
24(W)	Resolution	3D	8×16×32	2	IEA : 16×64×32×1	8
					IMA : 4×16×32×8	8
19(S)		ER	32(p)×4	1	IEA: 128(16×64)×32×1	8
	ER	3D	8×16×32	2	IMA: 4×16×32×8	8
29(W)		ER	32×64×4	2	IEA: 16×64×32×1	8
		3D	8×16×32	2	IMA: 4×16×32×8	8

"(S)" and "(W)" in the "No." column stand for solar wind mode and wake mode. "ER" in the "Mode Name" and "ER/3D" columns stands for electron reflectometer. "P", "Az", "E" and "M" in the "Electron Data" and "Ion Data" columns stand for polar angle, azimuthal angle, energy and mass. "Te" and "Ti" stand for time resolution of electron measurements and ion measurements, respectively. "(p)" shown in the "Electron Data" column stands for pitch angle distribution

commands. The time resolution of the electrons was as high as 2 seconds with 4 polar and 16 azimuthal angular sectors. In Mode 14, IEA sent 128 angular sectors out of 1024 angular sectors with the hemispherical FOV divided into 16 polar and 64 azimuthal sectors. The 128 angular sectors selected were centered in the solar wind direction. IMA sent only 8 mass species that corresponded to 8 predefined TOF ranges determined by pre-flight calibration. Mode 19(29) is called "ER Mode". "ER" stands for Electron Reflectometer and this mode is optimized for detecting magnetic anomalies on the lunar surface using ESA-S1 and ESA-S2 as an electron reflectometer. Mode 19 was optimized for dayside observation while Mode 29 was optimized for nightside observation. In Mode 19, high-angular resolution electron data (hemispherical FOV divided into 16 polar and 64 azimuthal sectors) were pitch-angle sorted (32 pitch angle directions) by SI-OBC (see Fig. 2) and the pitch-angle sorted data were sent with a maximum time resolution of 1 second. On the other hand, in Mode 29, high-angular resolution electron data (16 polar and 64 azimuthal sectors) were sent without pitch angle sorting on the spacecraft. In order to realize a high time resolution, only 4 energy steps were swept in Modes 19 and 29. In these modes, two second time resolution 3-D electron data (4 polar and 16 azimuthal angular sectors) were also sent every 60 seconds.

4 Operation and Flight Performance of the PACE Sensors

4.1 Flight Operation of the PACE Sensors

The PACE sensors were switched on about two months after launch. After a successful functional check of the low voltage part, the high voltage power supplies were switched on. The high applied voltage was gradually raised to the observation level over about a week. On 14 December 2007, MAP-PACE started continuous observation of the plasma around the Moon.

During the first 5 months of the MAP-PACE observation (from December 2007 to May 2008), we mainly used Mode 11 and Mode 12 switching between these modes every 24 hours. During the rest of the mission, 4 operation modes, Mode 11, Mode 12, Mode 14(24), and Mode 19(29), were switched after every 6 revolutions around the Moon corresponding to ∼12 hours. During the period that meteor showers were predicted to be observed, we alternated between Mode 11 and Mode 12 every 6 revolutions in order to obtain a detailed mass profile.

In order to monitor the degradation of the MCPs, we performed an MCP check by monitoring the count rate while changing the high voltage applied to the MCPs. The MCP check was performed every month during the first 5 months. Since the degradation of the MCPs slowed down 5 months after PACE commenced continuous observation, the MCP check was performed less frequently after May 2008.

4.2 Performance of Electrical Sensitivity Attenuation of IEA

Since the fluxes of solar wind ions and of ions coming from the Moon differ significantly, IEA and IMA had a function to reduce the sensitivity continuously down to 1/100 using the sensitivity control electrodes when observing solar wind ions. Although both IEA and IMA were equipped with this function, we applied the sensitivity attenuation only to IEA. The detailed design and laboratory experiment of the sensitivity control is described in Yokota et al. (2005). Although the sensitivity could be controlled continuously down to 1/100, we used only one predefined sensitivity reduction ratio of ∼1/50 during the flight operation since it would have taken quite a long time to calibrate the instrument before launch if we used multiple reduction ratios. Figure 16 shows the performance of the sensitivity control. We compared the solar wind ions observed by IEA with and without sensitivity attenuation. Before 1412 UT, sensitivity attenuation was disabled using “ENERGY SWEEP RAM No.1”. After 1412 UT, sensitivity attenuation was enabled by changing the energy sweep mode to “ENERGY SWEEP RAM No.0”. Note that the energy sweep range also changed when sensitivity attenuation was enabled. Figure 16 compares the energy versus differential energy flux before (red line) and after (blue line) enabling sensitivity attenuation. We attenuated the sensitivity below 2.4 keV/q. Based on the pre-flight calibration, an attenuation factor of 1/30 ∼ 1/50 (depending on energy and angular direction) was expected when enabling the sensitivity attenuation. We can see no significant discontinuity in the energy spectrum below and above 2.4 keV/q when the measured counts are converted into differential energy flux using the geometrical factor obtained during the pre-flight calibration. It is also clear that without sensitivity attenuation, IEA was saturated when measuring the solar wind.

4.3 Performance of UV Rejection

In order to reduce the solar UV photons entering the detectors (MCPs), serrations were made on the outer spheres where the first collision of any UV photons entering the detector

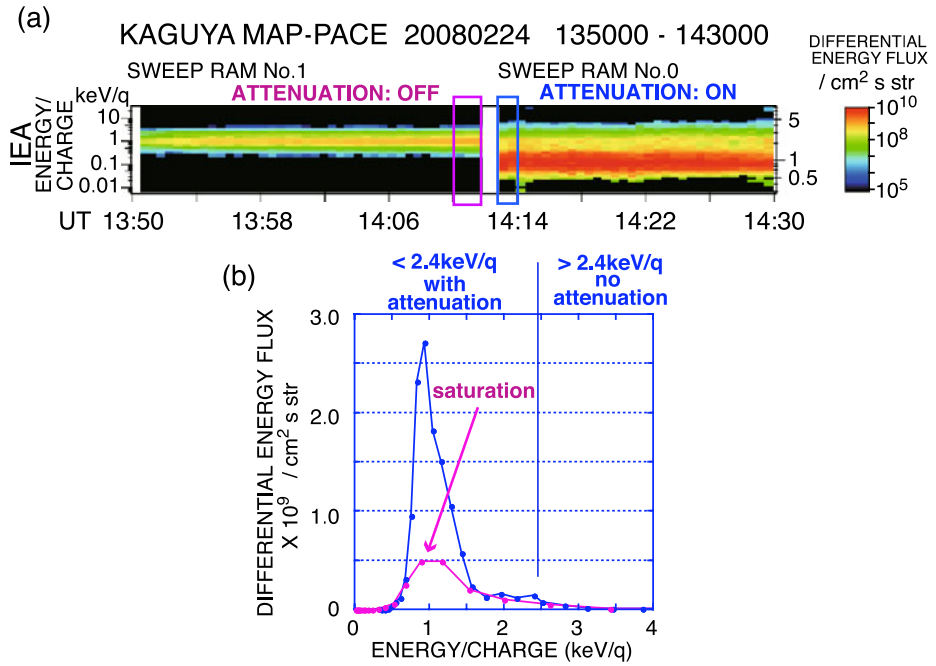

Fig. 16 Performance of the sensitivity control of IEA. *Red* (*blue*) line in panel (**b**) shows differential energy flux of solar wind ions during the time interval indicated by the *red* (*blue*) box in an E-t spectrogram of IEA in panel (**a**)

would occur. Besides the serrations, spherical/toroidal analyzers were blackened using carbon paint. We measured the analyzer response to UV photons using a deuterium lamp during the pre-flight calibration. According to the measured UV response, we expected UV photons to be detected when they entered the analyzer from the center of the field of view (which is inclined at 45 deg to the axis of symmetry). Since ESA-S1 and IMA always faced the Moon, solar UV photons did not directly enter ESA-S1 and IMA. Although this depended on the angle of the sun relative to the orbital plane, solar UV photons entered ESA-S2 and IEA once or twice per orbit with a duration shorter than a few minutes. The peak solar UV contamination on orbit turned out to be as low as 95 counts/s for ESA-S2 and 90 counts/s for IEA. Taking into account the geometrical factor and detection efficiency, the UV contamination of ESA-S2 was of the order of 10^6 $cm^{-2}\,s^{-1}\,str^{-1}$, while that of IEA was of the order of 10^7 $cm^{-2}\,s^{-1}\,str^{-1}$ (when attenuation was on). Since the differential energy flux of the solar wind electrons and ions was usually much higher, the UV contamination was acceptable for electron/ion measurements.

4.4 LEF High Voltage Operation and Mass Identification Performance of IMA

IMA is an LEF TOF mass spectrometer. In order to minimize angular scattering and energy straggling caused by the carbon foil, ions that passed through the energy analyzer were post accelerated by a high negative voltage before entering the carbon foil. On the other hand, positive ions that passed through the carbon foil were reflected by a high positive voltage, which was arranged so that the electric field intensity in the mass spectrometer was proportional to the distance from the carbon foil. Although the upper and lower limits of the

Table 8 IMA LEF high voltage operation

LEF high voltage level	Period
±8 kV	18 Jan. 2008 ∼ 24 Mar. 2008
±10 kV	24 Mar. 2008 ∼ 24 May 2008
±12 kV	24 May 2008 ∼ 3 Jun. 2009
±15 kV	3 Jun. 2009 ∼ 10 Jun. 2009

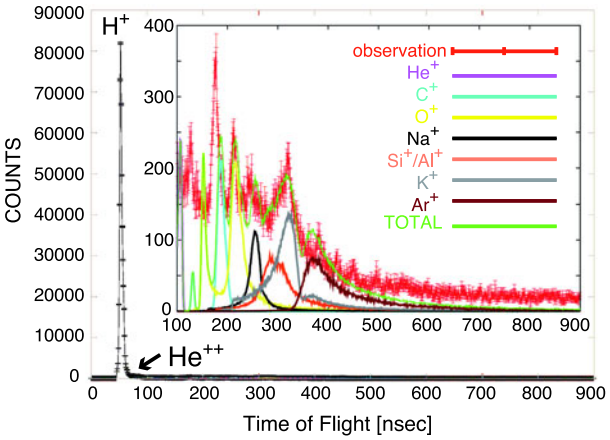

Fig. 17 TOF mass profile of IMA obtained by applying ±12 kV to the LEF register. The TOF profile was obtained by integrating the observed counts between 20 eV/q and 5 keV/q for one month (September 2008) when IMA was operated in TOF profile mode (see Table 7). The TOF measurement range of 1000 ns was divided equally into 1024 channels with a time resolution of 977 ps. The TOF profile shown has reduced the time resolution to 3.9 ns by summing up every 4 channels (the TOF measurement range of 1000 ns is divided equally into 256 channels). Since the counts of protons and alpha particles are much larger than heavier ions, only the large peak of protons and much smaller peak of alpha particles can be seen on the linear scale. The *inset* shows an enlarged TOF profile between 100 ns and 900 ns to focus on the TOF profile of heavy ions. The *red line* is the observed TOF profile with statistical error bars of 68% confidence level. The other colored lines are simulated TOF profiles. Assuming that He^+, C^+, N^+, O^+, Na^+, Al^+/Si^+, K^+ and Ar^+ are the contributing species, the simulated TOF profiles are chi-square fitted to the observed TOF profile. The *green line* is the summation of all the simulated profiles

high positive and negative voltages were ±15 kV, we operated IMA with ±12 kV during most of the flight operation period. Before turning on the LEF high voltage, we powered on a baking heater attached to the mass analyzer part of IMA (see Fig. 5) so that outgassing from the LEF cylinder should be quickened. In order to prevent an electric discharge being caused by outgassing from the spacecraft, especially during the initial phase after the launch, we started by applying ±8 kV to the mass spectrometer and gradually increased the voltage to ± 10 kV, ± 12 kV, and ± 15 kV. Table 8 shows the high voltage level and the period during which the voltage level was applied. Figure 17 shows an example of the TOF mass profile obtained by applying ±12 kV to the LEF register. Although we found some noise peaks, good enough in-flight mass identification performance was achieved for the observation of ions coming from the Moon.

4.5 In-flight Calibration

Although we calibrated the PACE sensors before launch, an absolute on-ground calibration was quite difficult. In order to obtain the absolute value of density, an in-flight calibration is important. We calculated the velocity moments including density from data obtained with the PACE sensors. Since plasma waves are sometimes emitted at the electron plasma frequency on the dayside of the Moon, we compared the density calculated from the PACE sensors with the density measured by the plasma wave instrument (LRS) on SELENE (Ono et al. 2008; Kasahara et al. 2008) and calculated the efficiency of the PACE sensors. Although the comparison is in progress, the resultant efficiency of the PACE sensors varies depending on the degradation of the MCPs. The calculated efficiency will be available to the public within the archived data in the future.

Since the field of view of the PACE sensors was a hemisphere, it was impossible to install all the PACE sensors on the spacecraft without blocking their field of view. Although the field of view of ESA-S1 and IMA was free from other spacecraft structures, the field of view of ESA-S2 and IEA was partly blocked by the high-gain antenna (HGA). Since one of the purposes of IEA was to continuously monitor the solar wind, we installed IEA so that HGA should not block the solar wind ion flow before being detected by IEA. Using the data obtained, we confirmed that there was no problem in measuring the solar wind ions throughout the observation period.

5 Data Archive

The raw telemetry data received at ground stations were de-packetized and stored in the SELENE database (SELENE Level-1 data). We processed the raw telemetry data of the PACE sensors and produced scientific data with multiple formats as SELENE Level-2 data. This processing included: (1) decompression of the data, (2) correction of the time, (3) subtraction of background noise data, and (4) formatting of data according to the PACE Level-2 data format. Table 9 shows the PACE Level-2 science data products that are registered in the SELENE database. The SELENE database was opened to the public in November 2009, one year after the end of the nominal mission operation. One of the PACE Level-2 science data products, PACE_ET1 is a 1 day summary plot of an electron/ion E-t spectrogram that has nearly the same format as Fig. 30. Currently, not all the PACE Level-2 science data products are registered since data products such as the magnetic anomaly map and secondary ion/scattered map require intensive data analysis before they are ready to be registered.

6 Low-Energy Ion Population on the Dayside of the Moon

6.1 Summary of Low-Energy Ion Population on the Dayside of the Moon

Before showing the observed data, we will summarize the newly found low-energy ion population on the dayside of the Moon at 100 km altitude in Fig. 18. The newly found ion populations comprise the four following components: (1) Solar wind protons backscattered at the lunar surface, (2) Solar wind protons reflected by magnetic anomalies on the lunar surface, (3) Reflected/backscattered protons picked-up by the solar wind, and (4) Ions originating from the lunar surface/lunar exosphere. In the following subsections, we will describe these four populations in detail, showing the observed data of each population.

Table 9 PACE Level-2 science data products

Product Name	Description	Format	Time Resolution
PACE_PBF1	High Resoution Count Data of Electron/Ion Energy Spectrum	BINARY	1 s(min.)
PACE_CDF1	High Resoution Count Data of Electron/Ion Energy Spectrum	CDF	1 s(min.)
PACE_ET1	Summary Plot of Electron/Ion E-T Spectrogram	IMAGE	1 plot/day
PACE_ERMA_MAP	Magnetic Anomaly Map (Electron Reflectometer)	PDS	N.A.
PACE_SI_MAP	Secondary Ion/Scattered Ion Map	PDS	N.A.

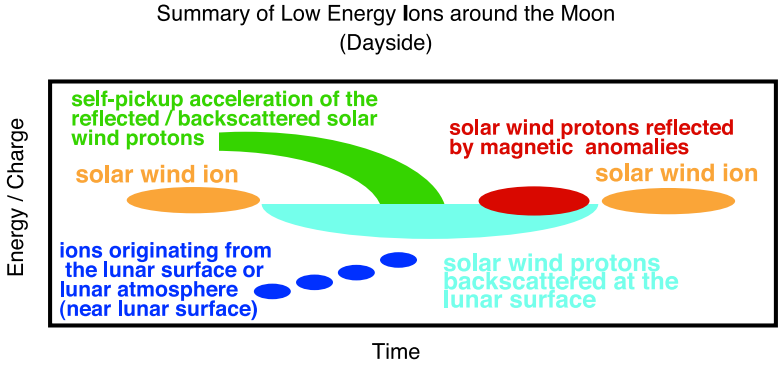

Fig. 18 Summary of low-energy ion population on the dayside of the Moon

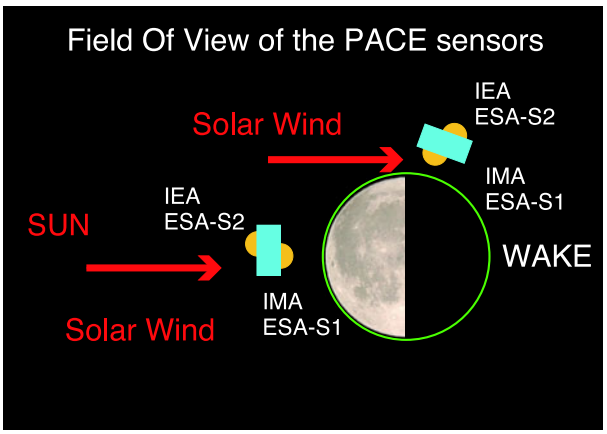

Fig. 19 Measurement configuration of PACE sensors

6.2 Solar Wind Ion Scattering at the Lunar Surface

The MAP-PACE ion sensors, IEA and IMA, found four clearly distinguishable characteristic low-energy ion populations on the dayside of the Moon. The first of these characteristic

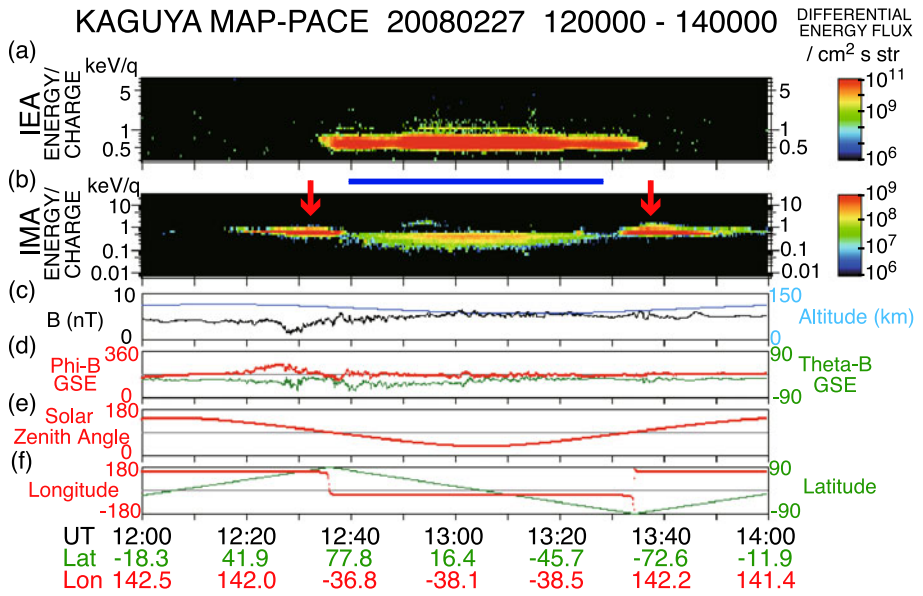

Fig. 20 An example of backscattered solar wind ions. Panels (**a**) and (**b**) are omni-directional E-t spectrograms from IEA and IMA. The *vertical scale* is the energy of ions while the *horizontal axis* is time. The color of each bin depicts the ion counts in each energy bin at the time of observations. IMA observed backscattered solar wind ions (during the time period indicated by a *horizontal blue line* between panels (**a**) and (**b**)) while IEA observed solar wind ions. The two *red arrows* indicate solar wind ions observed by IMA in the polar region. Panels (**c**) and (**d**) are altitude of SELENE, magnetic field intensity and direction in the Geocentric Solar Ecliptic (GSE) polar coordinate system. Panels (**e**) and (**f**) show the solar zenith angle and latitudinal/longitudinal position of SELENE in the Mean Earth/Polar Axis (ME) coordinate system

ion populations are solar wind ions backscattered at the lunar surface (Saito et al. 2008b). Instead of being perfectly absorbed by the lunar surface, about 0.1% to 1% of the incident solar wind ions were backscattered. Before showing the data, we will briefly explain the measurement configuration of the PACE sensors shown schematically in Fig. 19. Since ESA-S1 and IMA were installed on the spacecraft panel facing the Moon surface, ESA-S1 and IMA mostly measured electrons and ions propagating away from the Moon. On the other hand, ESA-S2 and IEA which were installed on the opposite spacecraft panel mostly measured electrons and ions going towards the Moon. Note that solar wind ions were detected by IEA or IMA depending on the position of the spacecraft. While IEA measured solar wind ions on the dayside, IMA measured solar wind ions near the day-night terminator line. Figure 20 shows an example of the backscattered ions (during the time period indicated by a horizontal blue line between panels (a) and (b)). The backscattered ions had lower energy than the incident solar wind ions since part of the energy was lost when solar wind ions collided with the Moon. Although the solar wind consists of alpha particles as a second major component, it was found that the backscattered ions consisted of almost no alpha particles (Saito et al. 2008b). The upper limit of the alpha particle flux was 0.1% of the backscattered proton flux. We also found a relationship between the lowest energy end of the backscattered ions and the latitude where the backscattered solar wind ions were observed. While the maximum energy of these ions was constant at slightly lower than the solar wind proton energy, the width of the energy distribution varied gradually, so that the minimum energy was larger at high latitudes than at the equator. Since the detail of the solar

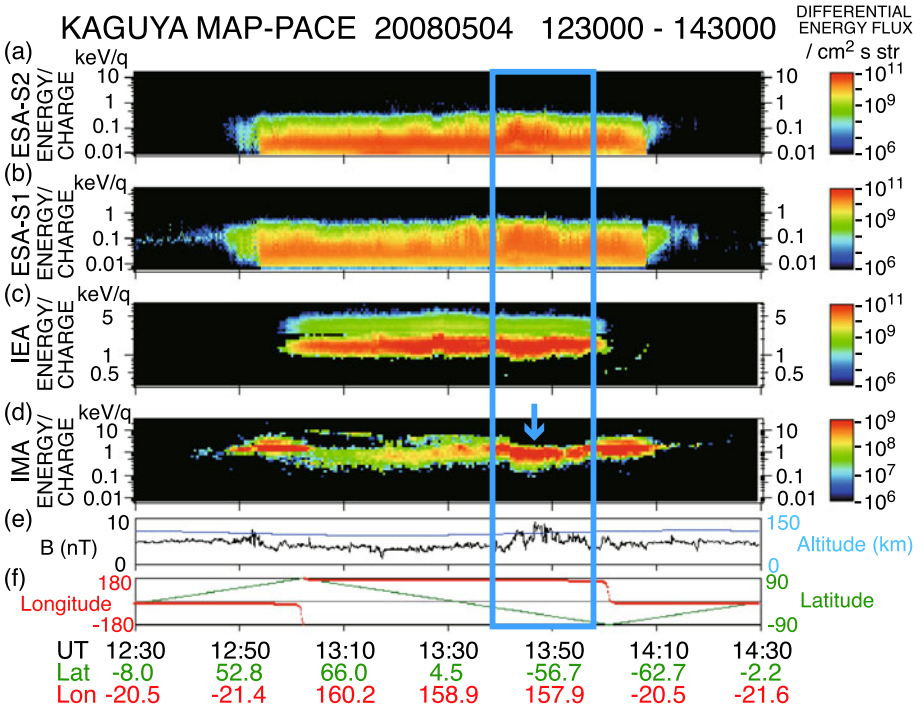

Fig. 21 Magnetically reflected solar wind ions observed at ∼100 km. Panels (**a**)–(**d**) are omni-directional E-t spectrograms from the PACE sensors. Panel (**e**) shows altitude of SELENE and magnetic field intensity. Panel (**f**) shows the latitudinal/longitudinal position of SELENE in the Mean Earth/Polar Axis (ME) coordinate system. Magnetically reflected solar wind ions were observed by IMA (indicated by a *blue arrow*) especially when SELENE flew over magnetic anomalies during the time period indicated by a *blue box*

wind-lunar surface interaction is still unclear, a laboratory experiment simulating solar wind backscattering at the lunar surface as well as further data analysis of the MAP-PACE ion sensors are necessary in order to fully understand the backscattering of the solar wind ions at the lunar surface.

McComas et al. (2009) reported the first observation of neutral atoms from the Moon. They found lunar backscatter and neutralization of the solar wind by an ENA analyzer IBEX-hi on Interstellar Boundary Explorer (IBEX). Their result of ENA albedo for the Moon of ∼10% is consistent with an ion backscattering of 0.1% to 1%. Recently, Wieser et al. (2009) also reported that extremely high reflection rates of solar wind particles from regolith-covered lunar surfaces were measured by the Sub-keV Atom Reflecting Analyzer (SARA) instrument on the Indian Chandrayaan-1 spacecraft. According to their observations, up to 20% of the solar wind protons were reflected from the lunar surface back to space as energetic neutral hydrogen atoms with energies greater than 25 eV, which is consistent with the results of IBEX.

6.3 Solar Wind Ion Reflection by Magnetic Anomalies

When SELENE flew over the South Pole Aitken region, where strong magnetic anomalies exist, solar wind ions reflected by magnetic anomalies were observed. In contrast with the

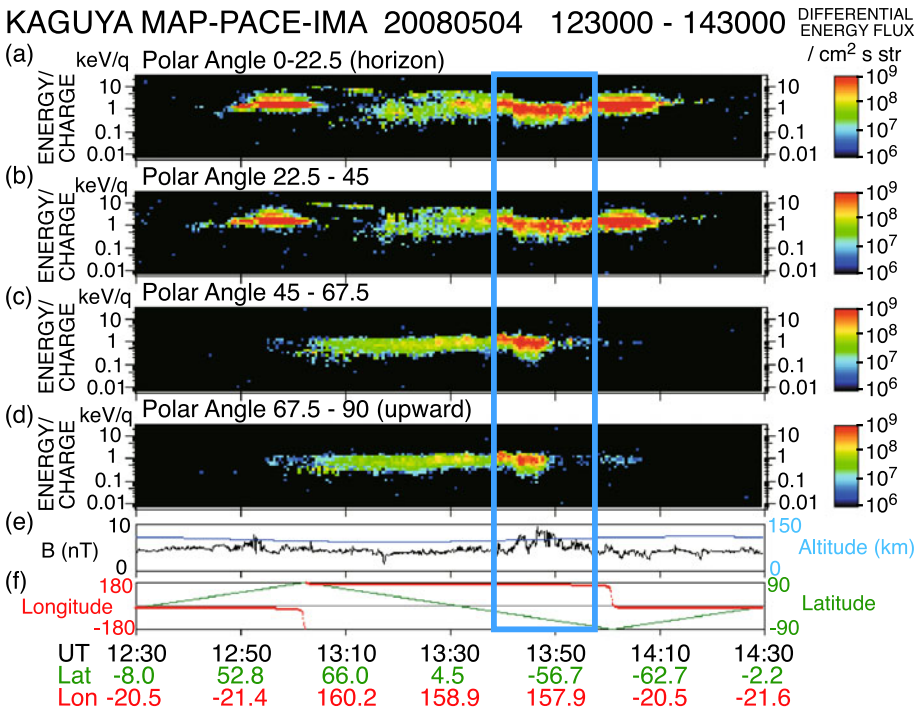

Fig. 22 E-t spectrograms of IMA with directional information when magnetically reflected solar wind ions were observed. Since IMA was operated in TOF profile mode (see Table 7), directional information about the azimuthal direction was not available. Panels (**a**)–(**d**) are E-t spectrograms of IMA for different polar angles. Panel (**e**) shows altitude of SELENE and magnetic field intensity. Panel (**f**) shows the latitudinal/longitudinal position of SELENE in the ME coordinate system. The *blue box* in the figure shows the period when magnetically reflected solar wind ions were observed

ions backscattered at the lunar surface, these magnetically reflected ions had nearly the same energy as the incident solar wind ions. Figure 21 shows an example of the magnetically reflected solar wind ions. When magnetically reflected ions were observed (indicated by a blue arrow), SELENE was at −20 deg ∼ −70 deg Latitude, 158.0 deg Longitude over the South Pole Aitken region. The flux of the magnetically reflected solar wind ions was much higher than the backscattered solar wind ions and was more than 10% of the incident solar wind ions. When magnetically reflected ions were observed, the electrons measured simultaneously were often heated and the incident solar wind ions were sometimes slightly decelerated. Figure 22 shows E-t spectrograms of four different polar angle directions of IMA. Since IMA was operated in the TOF profile mode, directional information relative to the azimuthal direction was not available (see Table 7). While backscattered solar wind ions were mainly observed in the polar angle above 45 deg (upward direction), magnetically reflected ions were observed in all the polar directions or at polar angles below 45 deg (horizontal direction) depending on the position of the spacecraft.

We also observed magnetically reflected ions at lower altitude of ∼40 km. Figure 23 shows an example of the magnetically reflected solar wind ions observed at ∼40 km. When these ions were observed (see blue arrows in the figure), SELENE was at −10 deg ∼ −80 deg Latitude, −162.0 deg Longitude. We found that backscattered solar wind ions

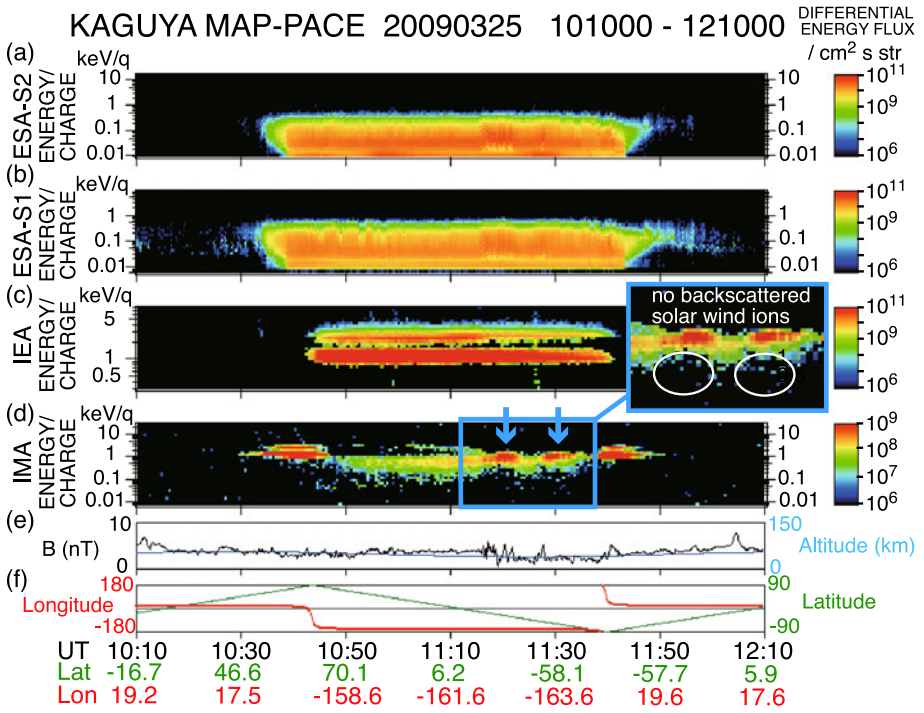

Fig. 23 Magnetically reflected solar wind ions observed at ~40 km. The format of the figure is the same as Fig. 21. Magnetically reflected solar wind ions were observed by IMA (indicated by *blue arrows*). When magnetically reflected solar wind ions were observed, the backscattered solar wind ions clearly disappeared as indicated by the *white circles in the inset*

clearly disappeared when magnetically reflected ions were observed as indicated by the white circles in the inset. This observation suggests that there exists lunar surfaces where magnetic anomalies protect the surface from solar wind ion bombardment. Figure 24 shows E-t spectrograms of four different polar angle directions of IMA. Since IMA was operated in the TOF profile mode, directional information relative to the azimuthal direction was not available. Although the backscattered solar wind ions were observed mainly at polar angles above 45 deg (upward direction), the high energy part of the backscattered solar wind ions can also be found at polar angles below 45 deg (horizontal direction). Magnetically reflected ions were observed in all the polar directions or at polar angles below 45 deg (horizontal direction), depending on the position of the spacecraft. Figure 25 shows schematically the difference between magnetically reflected solar wind ions and backscattered solar wind ions.

6.4 Pick-up Acceleration of the Backscattered/Reflected Solar Wind Ions

The third characteristic ion population found by the MAP-PACE ion sensors are ions accelerated over the solar wind energy. Since there exists a solar wind convection electric field seen from the Moon rest frame, the backscattered solar wind ions and magnetically reflected solar wind ions are accelerated by the electric field. Figure 26 shows an example of the accelerated ions (see white arrows in the figure). Saito et al. (2008b) showed the acceleration

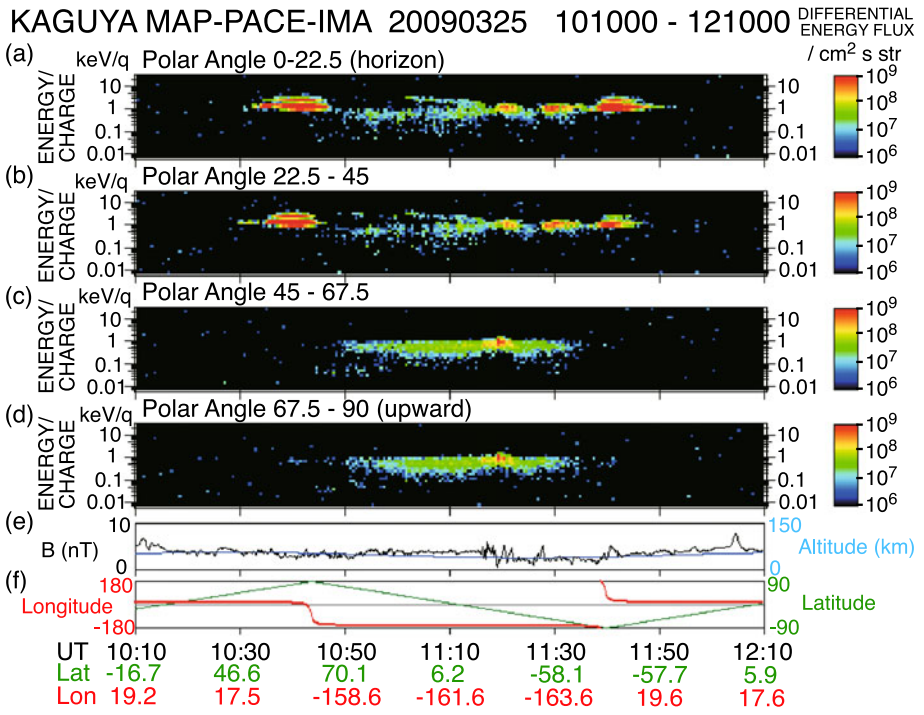

Fig. 24 E-t spectrograms from IMA with directional information when magnetically reflected solar wind ions were observed at ~40 km. Since IMA was operated in TOF profile mode (see Table 7), directional information about the azimuthal direction was not available. Panels (**a**)–(**d**) are E-t spectrograms from IMA for different polar angles. Panel (**e**) shows altitude of SELENE and magnetic field intensity. Panel (**f**) shows the latitudinal/longitudinal position of SELENE in the ME coordinate system

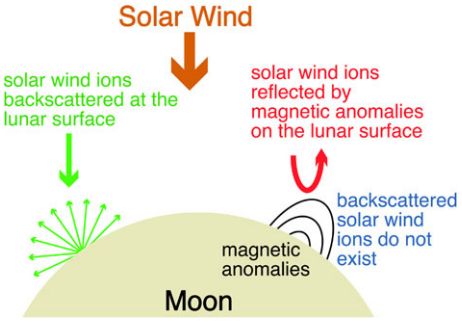

Fig. 25 Schematic diagram showing the difference between magnetically reflected solar wind ions and backscattered solar wind ions

of backscattered solar wind protons for the first time and they named the acceleration as "self-pickup acceleration". This acceleration process should be common to backscattered solar wind ions and magnetically reflected solar wind ions.

Since the backscattered/magnetically reflected solar wind ions have initial velocities that are lower than or equal to the incident solar wind ions, the maximum possible acceleration is three times the solar wind velocity, which is different from the pickup acceleration of the ionized neutral particles that have been observed around comets where the maximum

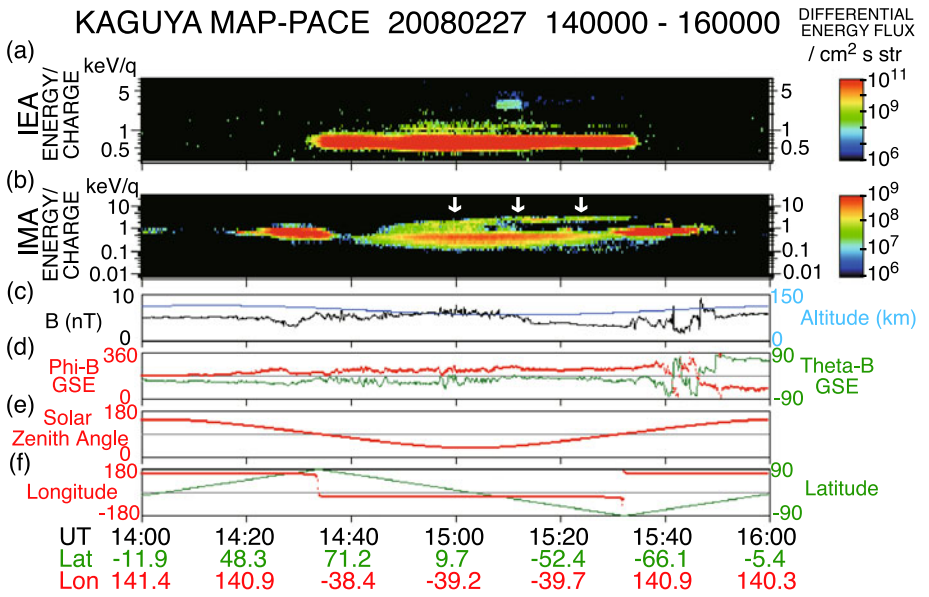

Fig. 26 An example showing self-pickup accelerated ions (indicated by white arrows). The format is the same as Fig. 20

acceleration is twice the solar wind velocity (Coates 2004; Mukai et al. 1986). Figure 27 shows schematically the self-pickup acceleration process.

We have simulated the self-pickup acceleration process using a simplified 2-D model. In this model, we have assumed that the solar wind proton energy is 750 eV corresponding to a solar wind velocity V of 380 km/s. The solar wind magnetic field B is perpendicular to the solar wind velocity and its intensity is 5 nT. The solar wind convection electric field $E = -V \times B$ is perpendicular to both the solar wind velocity and solar wind magnetic field and its intensity is 1.9 mV/m. We have ejected protons from IMA and back-traced ejected protons. Since IMA has a 2π str FOV facing the Moon, ions are ejected from IMA to the Moon. The ejected ions have energies between 100 eV/q and 7 keV/q every 100 eV/q. Some of the ejected ions reach the Moon surface. We have selected only the trajectories of ions that have energy below 750 eV/q (solar wind energy) on the lunar surface. Figure 28 shows the trajectories of the ions detected by IMA when SELENE is in the hemisphere where the solar wind convection electric field direction is from the lunar surface toward SELENE. The position of SELENE is indicated by a black circle. We have found that ions detected by IMA are grouped into two types: one are ions that are backscattered or magnetically reflected on the lunar surface far from the SELENE position and significantly accelerated by traveling a long distance (green trajectories in the figure) and the other are ions that are backscattered or magnetically reflected on the lunar surface near SELENE (red trajectories in the figure). The former ions have cycloidal trajectories that reach much higher altitudes than the SELENE orbit. The latter ions are flying in a nearly straight line from the lunar surface to IMA and are slightly accelerated by the solar wind convection electric field. The former ions correspond to self-pickup accelerated ions and the latter ions correspond to backscattered or magnetically reflected solar wind protons. Note that IMA can measure self-pickup accelerated ions from only a limited area of the Moon as determined by the solar wind convection electric field, solar wind magnetic field, and position of the spacecraft. Figure 29

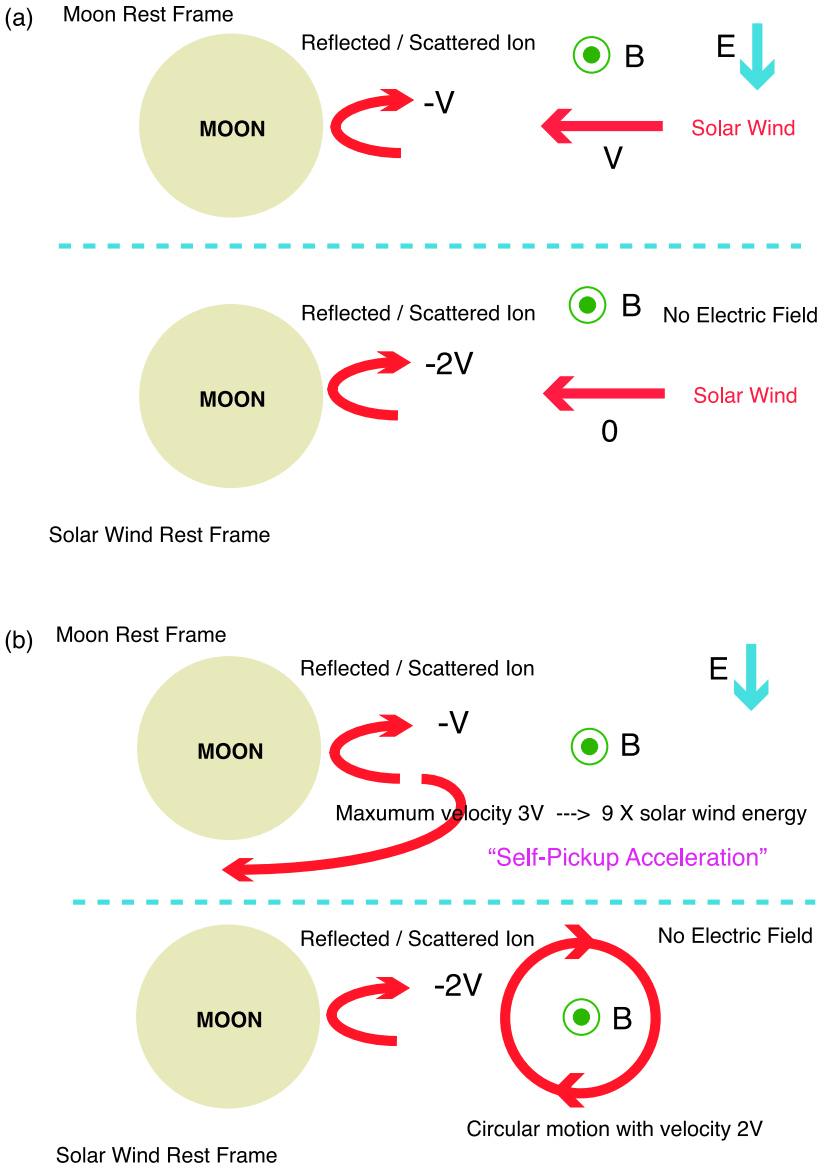

Fig. 27 Schematic diagram of the self-pickup acceleration process. (**a**) Seen from the Moon rest frame, solar wind ions backscattered or magnetically reflected at the lunar surface have maximum velocity $-V$ when the solar wind velocity is $+V$. Seen from the solar wind rest frame, the backscattered or magnetically reflected ions have maximum velocity $-2V$. (**b**) In the solar wind rest frame, the backscattered or magnetically reflected ions start undergoing a gyro-motion around the solar wind magnetic field with maximum velocity $+2$ V. When this gyro-motion is seen from the Moon rest frame, the motion is a cycloidal motion with maximum velocity of 3 V

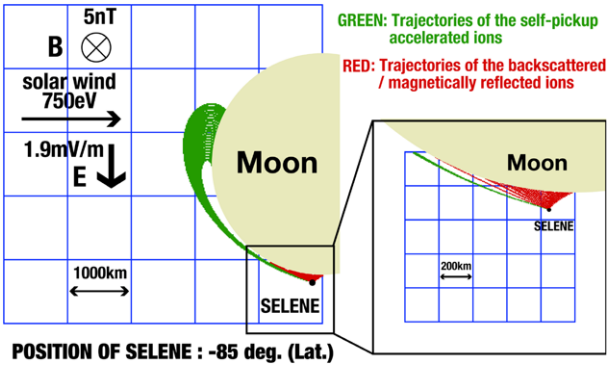

Fig. 28 2-D trajectories of the self-pickup accelerated ions and backscattered or magnetically reflected solar wind ions which are detected by IMA when SELENE is at −85 deg Latitude. *Green color* indicates trajectories of the self-pickup accelerated ions while *red color* indicates trajectories of the backscattered or magnetically reflected solar wind ions

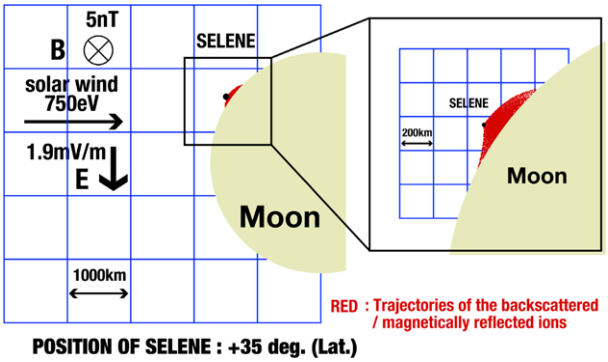

Fig. 29 2-D trajectories of the backscattered or magnetically reflected ions which are detected by IMA when SELENE is at +35 deg Latitude

shows the trajectories of ions detected by IMA when SELENE is in the hemisphere where the solar wind convection electric field direction is toward the lunar surface. We have found only ions that are backscattered or magnetically reflected on the lunar surface near SELENE (red trajectories in the figure).

6.5 Ions Originating from the Lunar Surface/Lunar Exosphere

Another important observation of IMA is the first *in situ* detection of alkali ions originating from the Moon surface/exosphere (Yokota et al. 2009). The ions generated on the lunar surface by solar wind sputtering, solar photon stimulated desorption, or micro-meteorite vaporization are accelerated by the solar wind convection electric field and detected by IMA. Figure 30 shows an example of the ions originating from the Moon surface/exosphere (indicated by the white box in the inset). These ions have the characteristic that the energy is lowest in polar regions (high latitude region) and their energy gradually increased as the spacecraft moved from the polar region to equator region. The ions were observed in only one of the hemispheres. These characteristics of the ion population could be explained as shown in Fig. 31. The source region of these ions was the dayside lunar surface or lunar exosphere. The ions generated were accelerated by the solar wind convection electric field. Since the acceleration distance was longer for the ions detected in the equatorial region than the ions detected in the polar region, the observed energy of the ions was higher in the equatorial region than in the polar region. The ions were not observed in one of the hemispheres because the direction of the solar wind convection electric field was toward the lunar surface in that hemisphere. Figure 32 shows the mass profile of these ions. We can find peaks for the

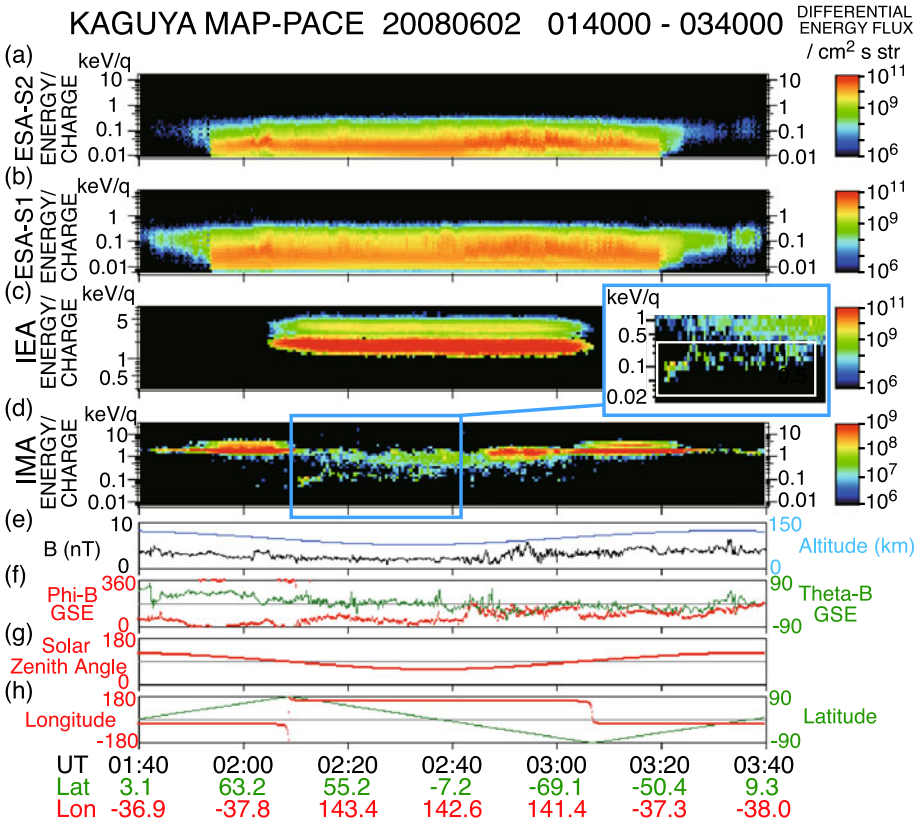

Fig. 30 Ions originating from the Moon surface/exosphere. Panels (**a**)–(**d**) are omni-directional E-t spectrograms from the PACE sensors. An inset shows the low-energy part of the enlarged IMA E-t spectrogram during the time period indicated by the blue box. Ions originating from the Moon surface/exosphere are indicated by the *white box in the inset*. Panels (**e**)–(**f**) show altitude of SELENE, magnetic field intensity and direction in GSE coordinates. Panels (**g**)–(**h**) show solar zenith angle and latitudinal/longitudinal position of SELENE in ME coordinates

heavy ions including C^+, O^+, Na^+, K^+ and Ar^+. Although the relation between the mass profile and the position of the spacecraft relative to the Moon surface is still under investigation, this observation will surely gives us new information about the generation mechanism of the lunar exosphere.

In addition to the observation of ions originating from the Moon surface/exosphere in the solar wind, IMA also found ions originating from the Moon surface/exosphere in the Earth's magnetosphere (Tanaka et al. 2009). Figure 33 shows an example of these ions (indicated by white arrows). These ions were observed when the Moon was in the magnetospheric lobe, on the dayside of the Moon. It was quite surprising that ions were generated in the lobe where no intense ion flux impacting the lunar surface such as the solar wind ion flux or plasma sheet ion flux existed. It clearly indicates that lunar alkali ions can be generated by mechanisms other than solar wind ion sputtering. It was also surprising that the ions originating from the Moon surface/exosphere were accelerated to SELENE in the lobe region where the convection electric field should be much weaker than in the solar wind. Figure 34 shows the mass profile of these ions. We can find peaks for the heavy ions including C^+,

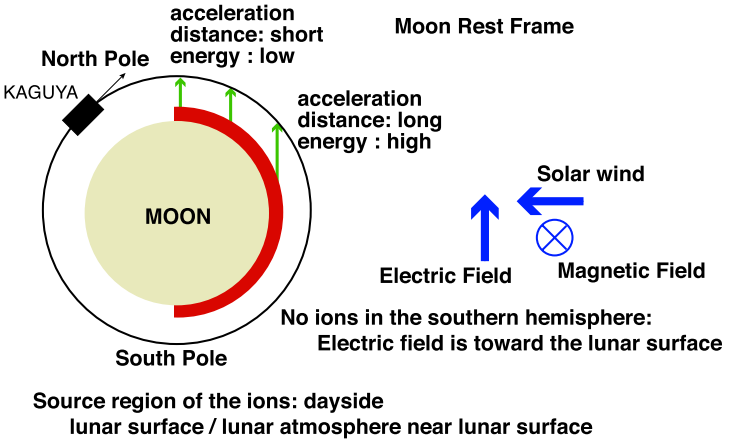

Fig. 31 Schematic diagram showing the generation and acceleration of ions originating from the Moon surface/exosphere

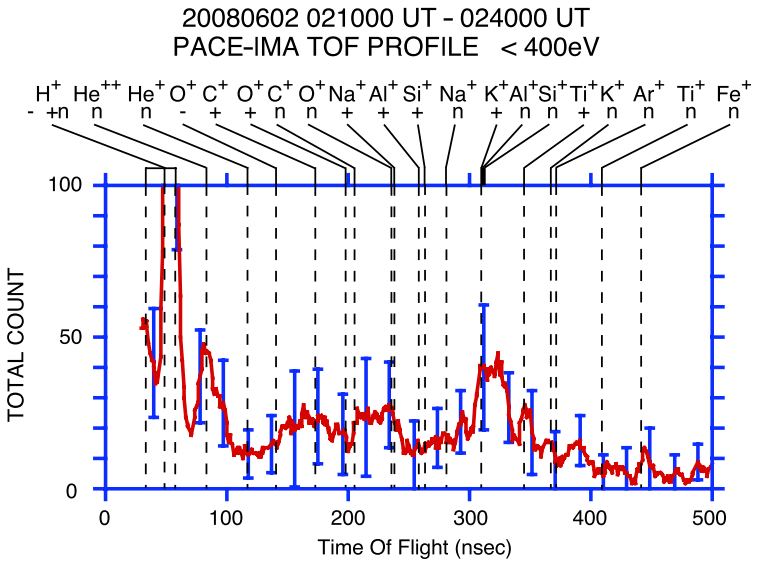

Fig. 32 Mass profile of the ions originating from the Moon surface/exosphere. The data below 400 eV/q obtained between 02:10:00 UT and 02:40:00 UT on 2 June 2008 are added up. The *red line* shows 10.7 nanosecond (11 data) running averaged TOF data with statistical error bars (*blue lines*) at 68% confidence level. The TOF of ions determined by laboratory calibration and/or numerical simulation are also shown. The letters "−", "+", and "n" below the ion species indicate the charge state of incident ions, negative, positive or neutral, respectively, after exiting the carbon foil. Although the TOF varies slightly with energy, the indicated TOF is for ions with energy of 100 eV/q

O^+, Na^+, K^+, and Ar^+ similarly to the ions originating from the Moon surface/exosphere observed in the solar wind. Figure 35 shows schematically that these ions were possibly accelerated by the potential difference between the lunar surface and SELENE. Both the lunar surface and SELENE are positively charged on the dayside of the Moon since photoelectron

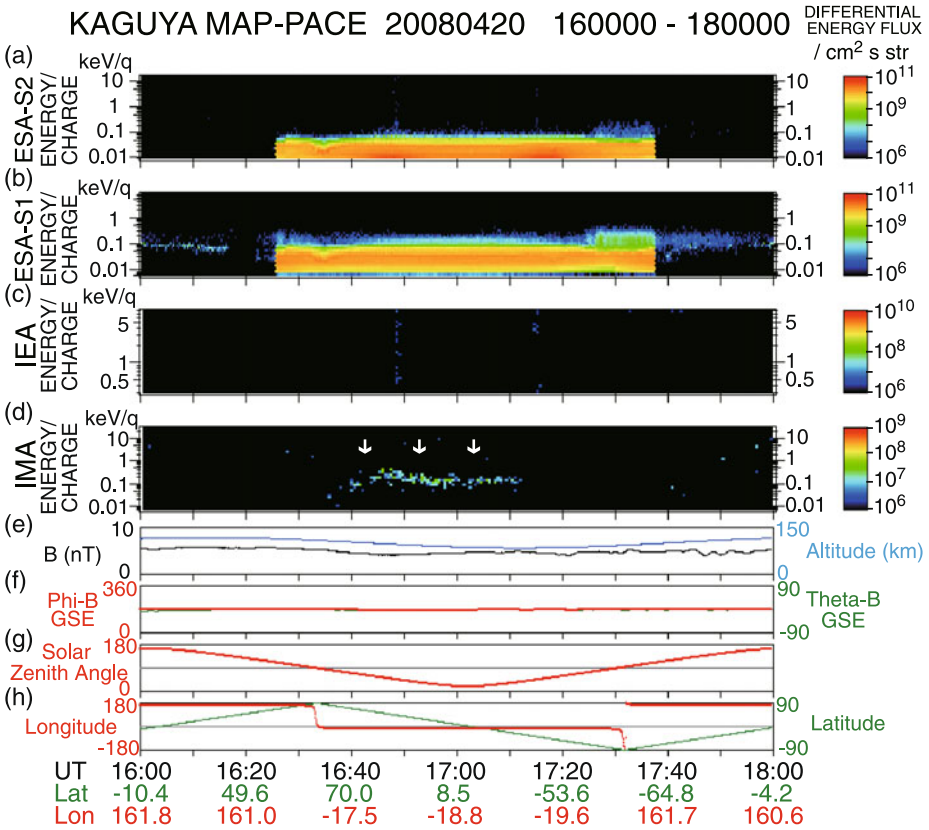

Fig. 33 Ions originating from the Moon surface/exosphere observed in the Earth's magnetosphere (lobe) (indicated by *white arrows*). The format is the same as Fig. 30

and electron currents are the major current sources and the photoelectron current dominates the current balance. Since the Debye length is larger than the spacecraft and much smaller than the Moon, it may be possible for the Moon surface to be positively charged to a higher potential than SELENE. If the acceleration was due to the potential difference between the lunar surface and SELENE, the lunar surface potential could be estimated from the energy of the measured ions and the photoelectron energy measured by the MAP-PACE-ESA sensors. In the case of the example shown in Fig. 33, the estimated lunar surface peak potential was about ∼440 V since the estimated spacecraft potential was ∼40 V and the peak energy of the measured ions that corresponded to the potential difference between the lunar surface and spacecraft was ∼400 V. Since a lunar surface potential of ∼440 V seems too high, there still exists some possibility that ions are generated by photo-ionization of exospheric neutrals and are accelerated by the convection electric field in the lobe region.

6.6 Discussion on Low-Energy Ion Population on the Dayside of the Moon

MAP-PACE-IMA found four new and different ion populations on the dayside of the Moon: (1) Solar wind protons backscattered at the lunar surface, (2) Solar wind protons reflected by magnetic anomalies on the lunar surface, (3) Reflected/backscattered protons picked-up

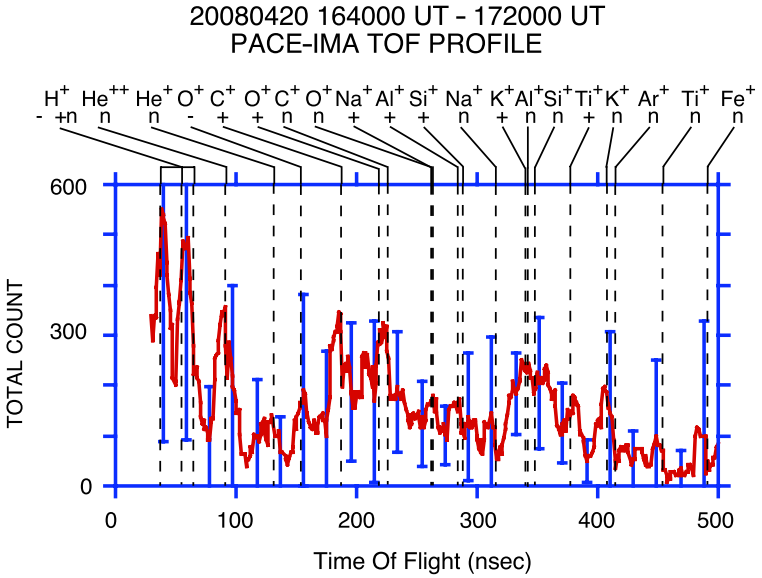

Fig. 34 Mass profile of the ions originating from the Moon surface/exosphere observed in the lobe. The data obtained between 16:40:00 UT and 17:20:00 UT on 20 April 2008 are added up. The *red line* shows 10.7 nanosecond (11 data) running averaged TOF data with statistical error bars (*blue line*) at 68% confidence level. The TOF of ions determined by laboratory calibration and/or numerical simulation are also shown. The letters "−", "+", and "n" below the ion species indicate the charge state of incident ions, negative, positive or neutral, respectively, after exiting the carbon foil. Although the TOF varies slightly with energy, the indicated TOF is for ions with energy of 100 eV/q

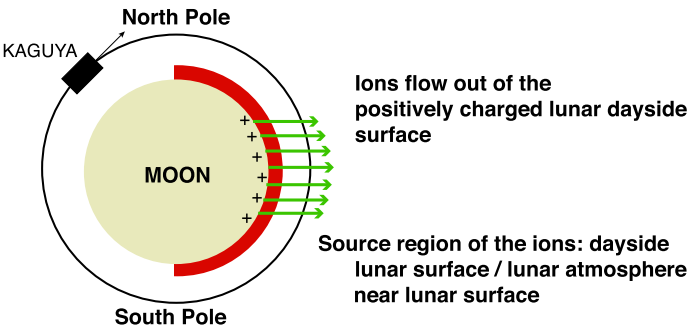

Fig. 35 Schematic diagram showing the generation and acceleration of ions originating from the Moon surface/exosphere

by the solar wind, and (4) Ions originating from the lunar surface/lunar exosphere. The ions originating from the lunar surface/lunar exosphere were observed in both the solar wind and in the Earth's magnetospheric lobe. In future we are planning to make a solar wind scattering map, quantitatively investigating the backscattered solar wind intensity and backscattering position on the lunar surface. Since the backscattered solar wind should contain information about the lunar surface, for example surface roughness, measurement of the backscattered solar wind may be a tool for remotely sensing the lunar surface using a natural ion beam:

the solar wind. We are also planning to investigate the relation between the ions originating from the lunar surface/lunar exosphere and the position where these ions are generated. This will also be a tool for remotely sensing lunar surface materials using the solar wind.

7 Conclusion

One of the scientific instruments on SELENE, MAP-PACE, has completed its ∼1.5 year observation of the low-energy charged particles around the Moon from a ∼100 km altitude (and below) polar orbit. All the PACE sensors performed quite well, as expected from the laboratory experiment carried out before launch. The newly observed data showed characteristic ion populations on the dayside of the Moon. Not limited to the dayside of the Moon, the MAP-PACE sensors also found new low-energy ion/electron populations in the lunar wake region (Nishino et al. 2009a, 2009b) and in the Earth's magnetotail (Nagai et al. 2009). By analyzing the data obtained in more detail, it is expected that many unresolved problems concerning the lunar plasma environment will be elucidated in the near future. Recently, two Asian Moon orbiters, Chinese Chang'E-1 and Indian Chandrayaan-1, have also made low-energy ion measurements around the Moon. Collaboration with these two missions will also lead to further understanding of the Moon plasma environment by multiple-point measurements of the low-energy ions around the Moon.

Acknowledgements The authors wish to express their sincere thanks to all the team members of MAP for their great support in processing and analyzing the MAP data. The authors also wish to express their grateful thanks to all system members of the SELENE project. The authors are greatly indebted to Dr. Yasuo Arai of High Energy Accelerator Research Organization for providing TDC chips that were indispensable for the TOF measurement of IMA. SELENE-MAP-PACE sensors were manufactured by Mitaka Kohki Co. Ltd., Meisei Elec. Co., Hamamatsu Photonics K.K., and Kyocera Co.

References

K.A. Anderson, L.M. Chase, R.P. Lin, J.E. McCoy, R.E. McGuire, J. Geophys. Res. **77**, 4611 (1972)
A.B. Binder, Science **281**, 1475 (1998)
C.W. Carlson, D.W. Curtis, G. Paschmann, W. Michael, Adv. Space Res. **2**, 67 (1982)
D.R. Clay, B.E. Goldstein, M. Neugebauer, C.W. Snyder, NASA Spec. Publ. **289**, 10-1 (1972)
A.J. Coates, Adv. Space Res. **33**, 1977 (2004)
D.S. Colburn, R.G. Currie, J.D. Mihalov, C.P. Sonett, Science **158**, 1040 (1967)
R.C. Elphic, H.O. Funsten, B.L. Barraclough, D.J. McComas, M.T. Paffett, D.T. Vaniman, G. Heiken, Geophys. Res. Lett. **18**, 2165 (1991)
B.H. Foing, G.D. Racca, A. Marini, E. Evrard, L. Stagnaro, M. Almeida, D. Koschny, D. Frew, J. Zender, J. Heather, M. Grande, J. Huovelin, H.U. Keller, A. Nathues, J.L. Josset, A. Malkki, W. Schmidt, G. Noci, R. Birkl, L. Iess, Z. Sodnik, P. McManamon, Adv. Space Res. **37**, 6 (2006)
Y. Futaana, S. Machida, Y. Saito, A. Matsuoka, H. Hayakawa, J. Geophys. Res. **106**, 18729 (2001)
Y. Futaana, S. Machida, Y. Saito, A. Matsuoka, H. Hayakawa, J. Geophys. Res. **108**, 1025 (2003)
J.S. Halekas, D.L. Mitchell, R.P. Lin, S. Frey, L.L. Hood, M.H. Acuna, A.B. Binder, J. Geophys. Res. **106**, 27841 (2001)
J.S. Halekas, D.L. Mitchell, R.P. Lin, L.L. Hood, M.H. Acuna, A.B. Binder, Geophys. Res. Lett. **29**(10) (2002). doi:10.1029/2001GL014428
J.S. Halekas, S.D. Bale, D.L. Mitchell, R.P. Lin, J. Geophys. Res. **110**, A07222 (2005). doi:10.1029/2004JA010991
J.S. Halekas, G.T. Delory, R.P. Lin, T.J. Stubbs, W.M. Farrell, J. Geophys. Res. **113**, A09102 (2008). doi:10.1029/2008JA013194
J.S. Halekas, G.T. Delory, R.P. Lin, T.J. Stubbs, W.M. Farrell, Planet. Space Sci. **57**, 78 (2009a). doi:10.1016/j.pss.2008.11.2009

J.S. Halekas, G.T. Delory, R.P. Lin, T.J. Stubbs, W.M. Farrell, J. Geophys. Res. **114**, A05110 (2009b). doi:10.1029/2009JA014113
M. Hilchenbach, D. Hovstadt, B. Klecker, E. Möbius, Adv. Space Res. **13**, 321 (1993)
H.K. Hills, J.C. Meister, R.R. Vondrak, J.W. Freeman Jr., NASA Spec. Publ. **289**, 12-1 (1972)
H.C. Howe, R.P. Lin, R.E. McGuire, K.A. Anderson, Geophys. Res. Lett. **1**, 101 (1974)
Y. Kasahara, Y. Goto, K. Hashimoto, T. Imachi, A. Kumamoto, T. Ono, H. Matsumoto, Earth Planets Space **60**, 341 (2008)
R.P. Lin, D.L. Mitchell, D.W. Curtis, K.A. Anderson, C.W. Carlson, J. McFadden, M.H. Acuna, L.L. Hood, A. Binder, Science **281**, 1480 (1998)
E.F. Lyon, H.S. Bridge, J.H. Binsack, J. Geophys. Res. **72**, 6113 (1967)
U. Mall, E. Kirsch, K. Cierpka, B. Wilken, A. Söding, F. Neubauer, G. Gloeckler, A. Galvin, Geophys. Res. Lett. **25**, 3799 (1998)
D.J. McComas, J.E. Nordholt, Rev. Sci. Instrum. **61**, 3095 (1990)
D.J. McComas, F. Allegrini, P. Bochsler, P. Frisch, H.O. Funsten, M. Gruntman, P.H. Janzen, H. Kucharek, E. Möbius, D.B. Reisenfeld, N.A. Schwadron, Geophys. Res. Lett. **36**, L12104 (2009). doi:10.1029/2009GL038794
T. Mukai, W. Miyake, T. Terasawa, M. Kitayama, K. Hirao, Nature **321**, 299 (1986)
T. Nagai, H. Tsunakawa, H. Shibuya, F. Takahashi, H. Shimizu, M. Matsushima, M.N. Nishino, Y. Yokota, K. Asamura, T. Tanaka, Y. Saito, O. Amm, Ann. Geophys. **27**, 59 (2009)
T. Nakagawa, Y. Takahashi, M. Iizima, Earth Planets Space **55**, 569 (2003)
M. Neugebauer, C.W. Snyder, D.R. Clay, B.E. Goldstein, Planet. Space Sci. **20**, 1577 (1972)
M.N. Nishino, K. Maezawa, M. Fujimoto, Y. Saito, S. Yokota, K. Asamura, T. Tanaka, H. Tsunakawa, M. Matsushima, F. Takahashi, T. Terasawa, H. Shibuya, H. Shimizu, Geophys. Res. Lett. **36**, L12108 (2009a). doi:10.1029/2009GL039049
M.N. Nishino, M. Fujimoto, K. Maezawa, Y. Saito, S. Yokota, K. Asamura, T. Tanaka, H. Tsunakawa, M. Matsushima, F. Takahashi, T. Terasawa, H. Shibuya, H. Shimizu, Geophys. Res. Lett. **36**, L16103 (2009b). doi:10.1029/2009GL039444
S. Nozette, P. Rustan, L.P. Pleasance, J.F. Kordas, I.T. Lewis, H.S. Park, R.E. Priest, D.M. Horan, P. Regeon, C.L. Lichtenberg, E.M. Shoemaker, E.M. Eliason, A.S. McEwen, M.S. Robinson, P.D. Spudis, C.H. Acton, B.J. Buratti, T.C. Duxbury, D.N. Baker, B.M. Jakosky, J.E. Blamont, M.P. Corson, J.H. Resnick, C.J. Rollins, M.E. Davies, P.G. Lucey, E. Malaret, M.A. Massie, C.M. Pieters, R.A. Reisse, R.A. Simpson, D.E. Smith, T.C. Sorenson, R.W. Vorder Breugge, M.T. Zuber, Science **266**, 1835 (1994)
K.W. Ogilvie, J.T. Steinberg, R.J. Fitzenreiter, C.J. Owen, A.J. Lazarus, W.J. Farrell, R.B. Torbert, Geophys. Res. Lett. **23**, 1255 (1996)
T. Ono, A. Kumamoto, Y. Yamaguchi, A. Yamaji, T. Kobayashi, Y. Kasahara, H. Oya, Earth Planets Space **60**, 321 (2008)
A.E. Potter, T.H. Morgan, Science **241**, 675 (1988)
A.E. Potter, R.M. Killen, T.H. Morgan, J. Geophys. Res. **105**, 15073 (2000)
Y. Saito, S. Yokota, K. Asamura, T. Tanaka, T. Mukai, Adv. Geosci. **7**, 33 (2007)
Y. Saito, S. Yokota, K. Asamura, T. Tanaka, R. Akiba, M. Fujimoto, H. Hasegawa, H. Hayakawa, M. Hirahara, M. Hoshino, S. Machida, T. Mukai, T. Nagai, T. Nagatsuma, M. Nakamura, K. Oyama, E. Sagawa, S. Sasaki, K. Seki, T. Terasawa, Earth Planets Space **60**, 375 (2008a)
Y. Saito, S. Yokota, T. Tanaka, K. Asamura, M.N. Nishino, M. Fujimoto, H. Tsunakawa, H. Shibuya, M. Matsushima, H. Shimizu, F. Takahashi, T. Mukai, T. Terasawa, Geophys. Res. Lett. **35**, L24205 (2008b). doi:10.1029/2008GL036077
H. Shimizu, F. Takahashi, N. Horii, A. Matsuoka, M. Matsushima, H. Shibuya, H. Tsunakawa, Earth Planets Space **60**, 353 (2008)
S.A. Stern, Rev. Geophys. **37**, 453 (1999)
F. Takahashi, H. Shimizu, M. Matsushima, H. Shibuya, A. Matsuoka, S. Nakazawa, Y. Iijima, H. Otake, H. Tsunakawa, Earth Planets Space **61**, 1269 (2009)
T. Tanaka, Y. Saito, AIP Conf. Proc. **1114**, 119 (2009). ISBN 987-92-9221-936-6
T. Tanaka, Y. Saito, S. Yokota, K. Asamura, M.N. Nishino, H. Tsunakawa, H. Shibuya, M. Matsushima, H. Shimizu, F. Takahashi, M. Fujimoto, T. Mukai, T. Terasawa, Geophys. Res. Lett. **36**, L22106 (2009). doi:10.1029/2009GL040682
M. Wieser, S. Barabash, Y. Futaana, M. Holmström, A. Bhardwaj, R. Sridharan, M.B. Dhanya, P. Wurz, A. Schaufelberger, K. Asamura, Planet. Space Sci. (2009). doi:10.1016/j.pss.2009.09.012
M. Wüest, D.S. Evans, R. von Steiger (eds.), ISSI Scientific Report Series (SR) Volume 7: Calibration of Particle Instruments in Space Physics, Appendix C Calibration Facilities (2007). ISBN 987-92-9221-936-6

S. Yokota, Y. Saito, Earth Planets Space **57**, 281 (2005)
S. Yokota, Y. Saito, Rev. Sci. Instrum. **79**, 013301 (2008). doi:10.1063/1.2829881
S. Yokota, Y. Saito, K. Asamura, T. Mukai, Rev. Sci. Instrum. **76**, 014501-1 (2005)
S. Yokota, Y. Saito, K. Asamura, T. Tanaka, M.N. Nishino, H. Tsunakawa, H. Shibuya, M. Matsushima, H. Shimizu, F. Takahashi, M. Fujimoto, T. Mukai, T. Terasawa, Geophys. Res. Lett. **36**, L11201 (2009). doi:10.1029/2009GL038185